J. Fluid Mech. (2014), *vol.* 744, *pp.* 404–429.
doi:10.1017/jfm.2014.50

Pilot-wave dynamics in a rotating frame: on the emergence of orbital quantization

Anand U. Oza, Daniel M. Harris, Rodolfo R. Rosales and John W. M. Bush†

Department of Mathematics, Massachusetts Institute of Technology, Cambridge, MA 02139, USA

(Received 1 August 2013; revised 1 August 2013; accepted 17 January 2014)

We present the results of a theoretical investigation of droplets walking on a rotating vibrating fluid bath. The droplet's trajectory is described in terms of an integro-differential equation that incorporates the influence of its propulsive wave force. Predictions for the dependence of the orbital radius on the bath's rotation rate compare favourably with experimental data and capture the progression from continuous to quantized orbits as the vibrational acceleration is increased. The orbital quantization is rationalized by assessing the stability of the orbital solutions, and may be understood as resulting directly from the dynamic constraint imposed on the drop by its monochromatic guiding wave. The stability analysis also predicts the existence of wobbling orbital states reported in recent experiments, and the absence of stable orbits in the limit of large vibrational forcing.

Key words: drops, Faraday waves, waves/free-surface flows

1. Introduction

At the 1927 Solvay Conference, Louis de Broglie presented a theory for quantum dynamics now commonly referred to as his double-wave pilot-wave theory (Bacciagaluppi & Valentini 2009). The theory postulates that quantum particles such as electrons are propelled, or 'piloted', by an extended wave field centred on the particle and generated by its internal vibration (de Broglie 1926, 1987). It was proposed that the resulting pilot-wave dynamics could give rise to the coherent wave-like statistical behaviour described by standard quantum theory. The theory thus postulates two waves, a real wave of unspecified origins responsible for guiding the particle, and the statistical wave describing the particle's probability density function. While such a physical picture provides a rational explanation for a number of quantum oddities, including single-particle diffraction (Bell 1988, p. 112), it was not widely accepted, instead being superseded by the Copenhagen Interpretation as the standard view. The first macroscopic pilot-wave system was recently discovered in the laboratory of Yves Couder (Couder *et al.* 2005; Protière, Boudaoud & Couder 2006; Couder & Fort 2006; Eddi *et al.* 2009; Fort *et al.* 2010).

Consider a fluid bath of density ρ, surface tension σ, kinematic viscosity ν and mean depth H, in the presence of a gravitational acceleration g, vibrating vertically

† Email address for correspondence: bush@math.mit.edu

with acceleration $\gamma\cos(2\pi ft)$. For $\gamma > \gamma_F$, γ_F being the Faraday threshold, a field of Faraday waves is excited on the surface. At the onset of instability, the period of the waves $T_F = 2/f$ is twice that of the vibrational forcing, and their wavelength $\lambda_F = 2\pi/k_F$ may be approximated by the water-wave dispersion relation (Kumar 1996),

$$(\pi f)^2 = \left(gk + \frac{\sigma k^3}{\rho}\right)\tanh kH. \tag{1.1}$$

When $\gamma < \gamma_F$, the interface remains flat unless perturbed, and the decay time of Faraday waves excited by a surface disturbance is $T_F M_e$. The non-dimensional 'memory parameter' M_e depends on the forcing acceleration γ according to

$$M_e(\gamma) = \frac{T_d}{T_F(1-\gamma/\gamma_F)}, \tag{1.2}$$

where T_d is the viscous decay time of the waves in the absence of forcing (Eddi *et al.* 2011; Moláček & Bush 2013*b*). The memory M_e increases progressively as the Faraday threshold is approached from below, as $\gamma \to \gamma_F$.

Walker (1978) demonstrated that fluid drops may be levitated above a vibrating fluid bath, their bouncing state enabled by the sustenance of an air layer between drop and bath during impact. Protière *et al.* (2006) experimentally characterized the dependence of the bouncing threshold γ_B on the system parameters, including the drop size. In certain regimes, there is a threshold for period-doubled bouncing γ_P, above which the drops bounce with the Faraday period T_F, so that their frequency is commensurate with that of the least-stable Faraday wave mode. For $\gamma > \gamma_W > \gamma_P$, γ_W being the walking threshold, the waves generated by the drop destabilize the bouncing state and propel it forward. The walking droplets, henceforth 'walkers', thus self-propel through a resonant interaction with their own wave field (Protière *et al.* 2006).

The walkers mimic quantum particles in several respects (Bush 2010). Eddi *et al.* (2009) observed that droplets can 'tunnel' through shallow fluid regions where walking is forbidden, which is reminiscent of electrons tunnelling through classically forbidden regions of high potential energy. In their study of single-particle diffraction, Couder & Fort (2006) reported that the statistical behaviour of walkers passing through single- and double-slit geometries resembles that of quantum particles. In the double-slit experiment, the droplet passes through one slit or the other, but is affected by its pilot-wave field that passes through both. Harris *et al.* (2013) revealed the emergence of wave-like statistics describing the position of a walker confined to a circular domain, which is reminiscent of the quantum corral experiments of Crommie, Lutz & Eigler (1993). It is worth noting that the walker's quantum-like behaviour only arises in the long-memory regime (Fort *et al.* 2010; Eddi *et al.* 2011). In the short-memory limit for walkers, $M_e \gtrsim M_e(\gamma_W)$, the standing waves generated by the drop decay relatively quickly, so the droplet motion depends only on its recent past. In the long-memory limit, $M_e \gg M_e(\gamma_W)$, the waves generated by successive bounces are long-lived, so the walker is more strongly influenced by its history. It is in this high-memory regime that the pilot-wave dynamics gives rise to a coherent wave-like statistics with characteristic wavelength λ_F (Couder & Fort 2006; Harris *et al.* 2013).

A theoretical description of the vertical motion of bouncing drops was developed by Moláček & Bush (2013*a*). A model for the coupled horizontal and vertical dynamics of walking drops was derived by Moláček & Bush (2013*b*), who rationalized the observed dependence of the walking threshold γ_W and the walking speed on the

system parameters. The model also predicted a number of new bouncing and walking states that have since been discovered experimentally (Wind-Willassen *et al.* 2013). In certain parameter regimes delineated by Moláček & Bush (2013*b*), the drop can walk steadily and stably at a uniform horizontal speed while bouncing vertically with the same period T_F as its guiding wave field. Such walkers with perfectly period-doubled vertical motion are henceforth referred to as 'resonant walkers'.

Oza, Rosales & Bush (2013) developed a pilot-wave model to describe the horizontal motion of resonant walkers. By time-averaging the full model of the coupled horizontal and vertical dynamics developed by Moláček & Bush (2013*b*), they derived an integro-differential trajectory equation to describe the horizontal motion of a resonant walker in the absence of boundaries and external forces. The model provides rationale for the observation that the bouncing state destabilizes into straight-line walking for $\gamma > \gamma_W$, and yields a formula for the walking speed that is consistent with experimental observations. The authors also analysed the stability of the steady walking state, and concluded that resonant walkers are stable to perturbations in the direction of motion, and neutrally stable to lateral perturbations. We here adopt their model in order to describe pilot-wave dynamics in a rotating frame.

2. Physical picture

We consider the behaviour of walkers on a circular bath of radius R_b rotating with angular frequency $\boldsymbol{\Omega} = \Omega\hat{\boldsymbol{z}}$ about its centreline, the physical system first considered by Fort *et al.* (2010). The centrifugal force on the bath will induce a parabolic deformation of the fluid interface of the form

$$h_0(r) = H - \frac{\Omega^2 R_b^2}{4g} + \frac{\Omega^2}{2g} r^2, \tag{2.1}$$

where H is the depth of the fluid at rest and r the radial distance from the rotation axis. Classically, a ball rolling with speed u_0 on a rotating frictionless parabolic table of height $h_0(r)$ will execute an inertial orbit of radius r_c, in which the radially outwards centripetal force mu_0^2/r_c is balanced by the inward Coriolis force $2m\Omega u_0$, so $r_c = u_0/2\Omega$. Fort *et al.* (2010) found that walkers on a rotating bath likewise execute circular orbits, and characterized the dependence of the orbital radii on the rotation rate Ω. In the low-memory limit, the walker's orbital radii decrease monotonically and continuously with Ω according to the formula $r_0 = au_0/2\Omega$, where $1.2 \leqslant a \leqslant 1.5$ is a fitting parameter. One contribution of this study will be to deduce a formula for the factor a and rationalize the difference between r_0 and r_c on physical grounds.

At high memory, Fort *et al.* (2010) demonstrated that the behaviour is markedly different: the orbital radius r_0 no longer varies continuously with Ω, and the orbital radii become quantized. The authors also report orbital degeneracy and hysteresis, in that two different orbital radii may be observed for the same rotation rate Ω, depending on whether Ω is approached from above or below. They suggest that the wave force on the drop in the high-memory regime reduces to that of a single diametrically opposed image source, proposing the governing equation

$$\frac{mu_0^2}{r_0} = \frac{2m\Omega u_0}{a} + K\cos(2k_F r_0), \tag{2.2}$$

where K is a constant. The range of validity of this approximation will be made clear in § 4.3.

As the Coriolis force $-2m\boldsymbol{\Omega} \times \dot{\boldsymbol{x}}_p$ on the walker in a rotating container is similar in form to the Lorentz force $-q\boldsymbol{B} \times \dot{\boldsymbol{x}}_p$ on an electron in a uniform magnetic field $\boldsymbol{B} = B\hat{\boldsymbol{z}}$ (Weinstein & Pounder 1945), Fort *et al.* (2010) propose a correspondence between the quantized orbits of walkers and Landau levels. They observe that in the high-memory regime, the quantized orbital radii approximately satisfy the relation

$$\frac{r_0}{\lambda_F} = \frac{b^2}{a}\left(n + \frac{1}{2}\right), \quad \text{for integer } n \geqslant 0, \tag{2.3}$$

where the prefactors $a \approx 1.5$ and $b \approx 0.89$ were deduced empirically. This is similar in form to the quantized Larmor radii r_{L} of an electron in a uniform magnetic field

$$\frac{r_{\mathrm{L}}}{\lambda_{\mathrm{dB}}} = \frac{1}{\pi}\left(n + \frac{1}{2}\right), \tag{2.4}$$

where λ_{dB} is the de Broglie wavelength. In § 4.3, we shall demonstrate that the quantized orbital radii in the high-memory regime are better approximated in terms of the zeros of the Bessel function $J_0(k_F r_0)$.

Eddi *et al.* (2012) examined two identical walkers orbiting each other in a rotating frame. The authors observed that the orbital radii of co-rotating orbits (orbits that rotate in the same sense as the fluid bath) increase with the rotation rate, while those of counter-rotating orbits decrease. The difference Δr depends linearly on the rotation rate Ω, which suggests an analogy with the Zeeman effect from quantum mechanics (Cohen-Tannoudji, Diu & Laloë 1977). An analogous level-splitting phenomenon will be explored here for the case of single walkers moving on circular orbits.

Harris & Bush (2014) presented the results of a comprehensive experimental study of walkers in a rotating frame, in which they observed a number of effects not reported by Fort *et al.* (2010). In particular, they found that orbital quantization only exists for a finite range of memory M_e. As M_e is progressively increased, the circular orbits destabilize into wobbling states, and subsequently into more complex trajectories. In the high-memory limit, the drop's trajectory becomes irregular, its radius of curvature oscillating erratically between those of accessible but unstable circular orbits. The histogram describing the trajectory's local radius of curvature thus takes a wavelike form, with peaks on the radii of the unstable orbital solutions. While the drop's trajectory is chaotic, the influence of the unstable orbital solutions is thus reflected in its wavelike statistical behaviour.

The goal of the current study is to use the approach developed by Oza *et al.* (2013) to examine the influence of rotation on the orbital motion of drops in a rotating frame. We here introduce the orbital memory parameter $M_e^O = T_F M_e / T_O$, where $T_O \approx 2\pi r_0/u_0$ is the walker's orbital period. In the high-orbital-memory regime $M_e^O \gg 1$, the drop completes an orbit before the local Faraday waves have decayed, thus interacting with its own wake. Its trajectory is thus strongly influenced by its history, as is stored in the wave field. We here rationalize the emergence of quantized orbits by assessing the linear stability of circular orbits. Moreover, we rationalize the observations of Harris & Bush (2014) that the circular orbits generally become unstable in the high-memory limit.

In § 3, we derive an integro-differential equation of motion for a drop in a rotating frame by adapting the model of Oza *et al.* (2013). In § 4, we study the dependence of the orbital radius on the rotation rate in various memory regimes, showing that the theoretical predictions compare favourably to recent experimental data (Harris & Bush 2014). The stability of the orbital solutions is analysed in § 5, which allows us to rationalize the emergence of quantized orbits in the intermediate memory regime, and their disappearance at high memory. Future directions are discussed in § 6.

3. Trajectory equation

Consider a drop of mass m and radius R_D walking on the surface of a fluid bath vibrating with vertical acceleration $\gamma\cos(2\pi ft)$. Let $\boldsymbol{x}_p(t) = (x_p(t), y_p(t))$ denote the horizontal position of the drop at time t. We assume the drop to be in a resonant state, so that its vertical motion is periodic with period $T_F = 2/f$. The horizontal force balance, time-averaged over the bouncing period, yields the equation of motion

$$m\ddot{\boldsymbol{x}}_p + D\dot{\boldsymbol{x}}_p = -mg\nabla h(\boldsymbol{x}_p, t) \tag{3.1}$$

(Oza *et al.* 2013), where the wave field generated by the walker is given by

$$h(\boldsymbol{x}, t) = \frac{A}{T_F}\int_{-\infty}^{t} J_0\left(k_F\left|\boldsymbol{x} - \boldsymbol{x}_p(s)\right|\right)\mathrm{e}^{-(t-s)/(T_F M_e)}\,\mathrm{d}s. \tag{3.2}$$

The drop experiences a propulsive wave force $-mg\nabla h(\boldsymbol{x}_p, t)$ and a time-averaged drag force $-D\dot{\boldsymbol{x}}_p$, where formulae for the amplitude A and time-averaged drag coefficient D are given in table 1 (Moláček & Bush 2013*b*). The first term in the formula for D results from the drag induced on the drop during impact, the second from its free flight. During each impact, the walker generates a monochromatic standing wave with spatial amplitude profile $J_0\left(k_F\left|\boldsymbol{x} - \boldsymbol{x}_p\right|\right)$ and decay time $T_F M_e$ (Moláček & Bush 2013*b*). We assume the wave field to be linear, so that $h(\boldsymbol{x}, t)$ may be expressed as the sum of the waves generated prior to time t. The wave field (3.2) is obtained by approximating the resulting discrete sum as an integral, an approximation that is valid provided the timescale of horizontal motion $T_H = \lambda_F/|\dot{\boldsymbol{x}}_p|$ is much greater than the timescale T_F of vertical motion, as is the case in the experiments. The Faraday wavenumber k_F is well approximated by (1.1), as the effect of the rotation on the dispersion relation is negligible in the regime of interest, $\Omega \ll f$.

We refer to (3.1)–(3.2) as the *stroboscopic approximation* since, by averaging over the vertical dynamics, we have eliminated consideration of the drop's vertical motion. The drop is thus effectively 'strobed' at the bouncing frequency, and approximated as a continuous moving source of standing waves. The richness of this pilot-wave system arises through the propulsive wave force $-mg\nabla h(\boldsymbol{x}_p, t)$ that depends explicitly on the walker's past. We note that the dominant contribution to the integral comes from its recent past, specifically $t - s \sim O(T_F M_e)$, so the drop is influenced by more of its history as the memory M_e increases.

If the container is forced below the walking threshold, the drop simply bounces in place, as the bouncing solution $\boldsymbol{x}_p \equiv$ constant is stable for $\gamma < \gamma_W$ (Oza *et al.* 2013). When forced above the walking threshold ($\gamma > \gamma_W$), the bouncing solution destabilizes into a stable walking solution $\boldsymbol{x}_p(t) = u_0 t(\cos\theta, \sin\theta)$, where the arbitrary angle θ determines the walking direction. The balance between the wave and drag forces determines the speed u_0. Formulae for γ_W and u_0 in terms of experimental parameters are provided in table 1 (Oza *et al.* 2013).

In a container rotating about its vertical centreline with angular frequency $\boldsymbol{\Omega} = \Omega\hat{\boldsymbol{z}}$, there are three additional physical effects. The drop experiences a Coriolis force $-2m\boldsymbol{\Omega}\times\dot{\boldsymbol{x}}_p$ and centrifugal force $-m\boldsymbol{\Omega}\times\left(\boldsymbol{\Omega}\times\boldsymbol{x}_p\right)$, fictitious forces arising when Newton's laws are written in the rotating frame. It also experiences an additional time-averaged propulsive force $-\overline{F(t)\nabla h_0(\boldsymbol{x}_p)}$ resulting from the parabolic deformation of the fluid interface, where $h_0(\boldsymbol{x})$ is given by (2.1) and $F(t)$ is the instantaneous vertical force acting on the drop. Since the drop's vertical motion is periodic, the average vertical force must equal the drop's weight, so $\overline{F(t)} = mg$ (Moláček & Bush 2013*b*). As the timescale of the drop's horizontal motion is much larger than the

Dimensional variables	**Definition**
$\boldsymbol{x}_p$	Drop position
m	Drop mass
R_D	Drop radius
ν	Fluid kinematic viscosity
ν_{eff}	Effective fluid kinematic viscosity (Moláček & Bush 2013*b*)
σ	Fluid surface tension
ρ	Fluid density
μ_a	Air dynamic viscosity
ρ_a	Air density
f	Forcing frequency
γ	Forcing acceleration
γ_F	Faraday instability threshold
g	Gravitational acceleration
$T_F = 2/f$	Faraday period
T_d	Decay time of waves without forcing
λ_F	Faraday wavelength
$k_F = 2\pi/\lambda_F$	Faraday wavenumber
Φ	Mean phase of wave during contact time
$D = 0.17mg\sqrt{\frac{\rho R_D}{\sigma}} + 6\pi\mu_a R_D\left(1 + \frac{\rho_a g R_D}{12\mu_{af}}\right)$	Drag coefficient
$A = \frac{1}{\sqrt{2\pi}}\frac{k_F R_D}{3k_F^2 R_D^2 + \mathscr{B}o}\frac{R_D k_F^2 \nu_{\text{eff}}^{1/2}}{\sigma\sqrt{T_F}} mgT_F \sin\Phi$	Amplitude of single surface wave
$F = mgAk_F$	Wave force coefficient
$\gamma_W = \gamma_F\left(1 - \sqrt{\frac{Fk_F T_d^2}{2DT_F}}\right)$	Walking threshold
$u_0 = \frac{1}{k_F T_d}\left(1 - \frac{\gamma}{\gamma_F}\right)\left\{\frac{1}{4}\left[-1 + \sqrt{1 + 8\left(\frac{\gamma_F - \gamma_W}{\gamma_F - \gamma}\right)^2}\right]^2 - 1\right\}^{1/2}$	Walking speed
$\boldsymbol{\Omega} = \Omega\hat{\boldsymbol{z}}$	Angular frequency of fluid bath
r_0	Orbital radius
ω	Orbital frequency
Non-dimensional variables	
$\mathscr{B}o = \frac{\rho g R_D^2}{\sigma}$	Bond number
$M_e = \frac{T_d}{T_F(1-\gamma/\gamma_F)}$	Memory
$\kappa = \frac{m}{DT_F M_e}$	Non-dimensional mass
$\beta = \frac{Fk_F T_F M_e^2}{D}$	Non-dimensional wave force coefficient
$\hat{\boldsymbol{\Omega}} = \frac{2m\boldsymbol{\Omega}}{D}$	Non-dimensional angular frequency of fluid bath
$\hat{r}_0 = k_F r_0$	Non-dimensional orbital radius
$\hat{\omega} = \omega T_F M_e$	Non-dimensional orbital frequency
$M_e^O = \frac{\hat{\omega}}{2\pi}$	Orbital memory

TABLE 1. The variables appearing in the trajectory equations (3.3) and (3.4).

bouncing period, we may approximate $\overline{F(t)\nabla h_0(\boldsymbol{x}_p)}$ as $m\Omega^2\boldsymbol{x}_p$, which precisely cancels the centrifugal force. We thus obtain the integro-differential equation of motion

$$m\ddot{\boldsymbol{x}}_p + D\dot{\boldsymbol{x}}_p = \frac{F}{T_F}\int_{-\infty}^{t} \frac{J_1\left(k_F\left|\boldsymbol{x}_p(t)-\boldsymbol{x}_p(s)\right|\right)}{\left|\boldsymbol{x}_p(t)-\boldsymbol{x}_p(s)\right|}(\boldsymbol{x}_p(t)-\boldsymbol{x}_p(s))\mathrm{e}^{-(t-s)/(T_F M_e)}\,\mathrm{d}s - 2m\boldsymbol{\Omega}\times\dot{\boldsymbol{x}}_p, \tag{3.3}$$

where $F = mgAk_F$. We note that this equation simply corresponds to the pilot-wave trajectory equation (3.1) augmented by the Coriolis force.

We now non-dimensionalize (3.3) by introducing the dimensionless variables $\hat{\boldsymbol{x}} = k_F\boldsymbol{x}$ and $\hat{t} = t/(T_F M_e)$. Using primes to denote differentiation with respect to $\hat{t}$, the non-dimensional equation of motion becomes

$$\kappa\hat{\boldsymbol{x}}_p'' + \hat{\boldsymbol{x}}_p' = \beta\int_{-\infty}^{\hat{t}} \frac{J_1(|\hat{\boldsymbol{x}}_p(\hat{t})-\hat{\boldsymbol{x}}_p(\hat{s})|)}{|\hat{\boldsymbol{x}}_p(\hat{t})-\hat{\boldsymbol{x}}_p(\hat{s})|}(\hat{\boldsymbol{x}}_p(\hat{t})-\hat{\boldsymbol{x}}_p(\hat{s}))\mathrm{e}^{-(\hat{t}-\hat{s})}\,\mathrm{d}\hat{s} - \hat{\boldsymbol{\Omega}}\times\hat{\boldsymbol{x}}_p', \tag{3.4}$$

where $\kappa = m/DT_F M_e$, $\beta = Fk_F T_F M_e^2/D$ and $\hat{\boldsymbol{\Omega}} = 2m\boldsymbol{\Omega}/D$ represent, respectively, the non-dimensional mass, wave force coefficient and rotation rate. The variables appearing in (3.3) and (3.4) are listed in table 1. Note that the model has no free parameters: formulae for D and A are derived by Moláček & Bush (2013*b*), and T_d and γ_F can be determined numerically (Kumar 1996; Moláček & Bush 2013*b*). We proceed by examining the extent to which (3.3) describes the trajectory of a drop walking in a rotating frame.

4. Orbital solutions

We seek orbital solutions with constant radius $\hat{r}_0$ and orbital frequency $\hat{\omega}$, and so substitute $\hat{\boldsymbol{x}}_p = (\hat{r}_0\cos\hat{\omega}\hat{t}, \hat{r}_0\sin\hat{\omega}\hat{t})$ into (3.4). The integro-differential equation thus reduces to a system of algebraic equations that define $\hat{r}_0$ and $\hat{\omega}$ in terms of M_e and $\hat{\Omega}$:

$$\left.\begin{aligned} -\kappa\hat{r}_0\hat{\omega}^2 &= \beta\int_0^{\infty} J_1\left(2\hat{r}_0\sin\frac{\hat{\omega}z}{2}\right)\sin\frac{\hat{\omega}z}{2}\mathrm{e}^{-z}\,\mathrm{d}z + \hat{\Omega}\hat{r}_0\hat{\omega} \\ \hat{r}_0\hat{\omega} &= \beta\int_0^{\infty} J_1\left(2\hat{r}_0\sin\frac{\hat{\omega}z}{2}\right)\cos\frac{\hat{\omega}z}{2}\mathrm{e}^{-z}\,\mathrm{d}z. \end{aligned}\right\} \tag{4.1}$$

The predictions of (4.1) for the dependence of r_0 and ω on γ/γ_F and Ω are compared with the experimental data of Harris & Bush (2014) in figures 1 and 2. The theoretical predictions are generated as follows. The drop radius R_D determines the drag coefficient D (table 1). The dimensionless forcing acceleration γ/γ_F and the decay time $T_d \approx 0.0174$ s for 20.9 cSt oil (Moláček & Bush 2013*b*) determine the memory parameter M_e through (1.2). Using the formulae in table 1, the experimentally observed free walking speed u_0 is used to determine the wave amplitude A, which in turn determines the phase Φ. The values of $\sin\Phi$ so obtained are within 30 % of those reported in Moláček & Bush (2013*b*). Given the values of D, A and M_e, the non-dimensional parameters κ, β and $\hat{\Omega}$ are determined through the definitions in table 1. The algebraic equations (4.1) are then solved numerically, yielding the orbital radius r_0 and frequency ω as functions of Ω. In figures 1 and 2, stable orbital solutions are indicated in blue, while unstable orbital solutions are indicated in red and green. The rationale for the stability of the orbital solutions, and so the distinction between the blue, red and green regions, will be described in § 5.

The wave fields $h(\boldsymbol{x}, t)$ accompanying the orbiting drop, as computed on the basis of (3.2), are shown in figure 3. Note that interference effects in the wave field become

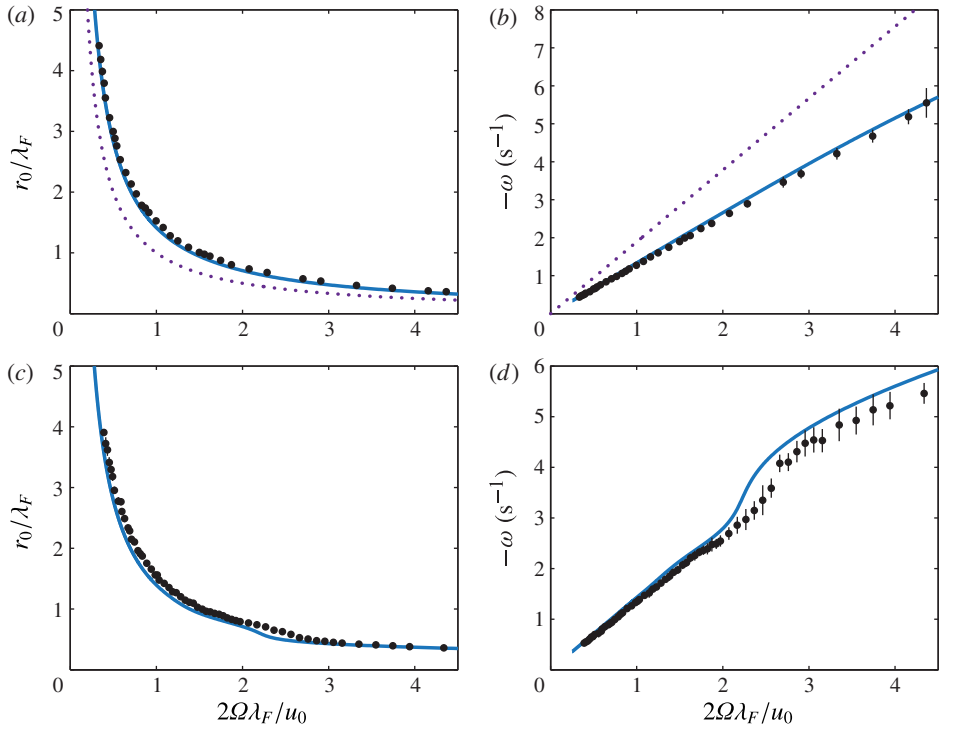

FIGURE 1. The predicted dependence of the orbital radius r_0 (*a*,*c*) and orbital frequency ω (*b*,*d*) on the bath's rotation rate Ω in the low-memory regime. The dotted lines represent the standard prediction for inertial orbits: (*a*) $r_0 = u_0/2\Omega$; (*b*) $\omega = -2\Omega$. The solid curves are the theoretical predictions determined by solving (4.1) with experimental parameters corresponding to the data reported by Harris & Bush (2014), who used a silicone oil of viscosity $\nu = 20.9$ cSt, density $\rho = 950$ kg m^{-3}, surface tension $\sigma = 0.0206$ N m^{-1} and forcing frequency $f = 80$ Hz. There are no fitting parameters. For (*a*,*b*), $\gamma/\gamma_F = 0.822$, free walking speed $u_0 = 9.0$ mm s^{-1} and drop radius $R_D = 0.4$ mm. For (*c*,*d*), $\gamma/\gamma_F = 0.922$, $u_0 = 9.5$ mm s^{-1} and $R_D = 0.4$ mm. Note that both r_0 and ω vary continuously with the rotation rate Ω.

more pronounced as the memory increases. We proceed by investigating the properties of these orbital solutions.

4.1. *Low orbital memory* $M_e^O \ll 1$

We first consider the low-orbital-memory regime $M_e^O \ll 1$, in which the drop's orbital period is much less than the decay time of the Faraday waves; consequently, the drop does not interact with its own wake. Since the dimensionless orbital frequency is $\hat{\omega} = \omega T_F M_e = 2\pi M_e^O$, we note that $M_e^O \ll 1$ is equivalent to $|\hat{\omega}| \ll 1$. In this limit, the defining equations (4.1) for the orbital radius and orbital frequency yield, to leading order in $\hat{\omega}$,

$$\left.\begin{aligned} -\kappa\hat{r}_0\hat{\omega}^2 - \hat{\Omega}\hat{r}_0\hat{\omega} &= \beta\left[\frac{\hat{\omega}}{2}\int_0^\infty zJ_1(\hat{r}_0\hat{\omega}z)\mathrm{e}^{-z}\,\mathrm{d}z + O(\hat{\omega}^3)\right], \\ \hat{r}_0\hat{\omega} &= \beta\left[\int_0^\infty J_1(\hat{r}_0\hat{\omega}z)\mathrm{e}^{-z}\,\mathrm{d}z + O(\hat{\omega}^2)\right]. \end{aligned}\right\} \tag{4.2}$$

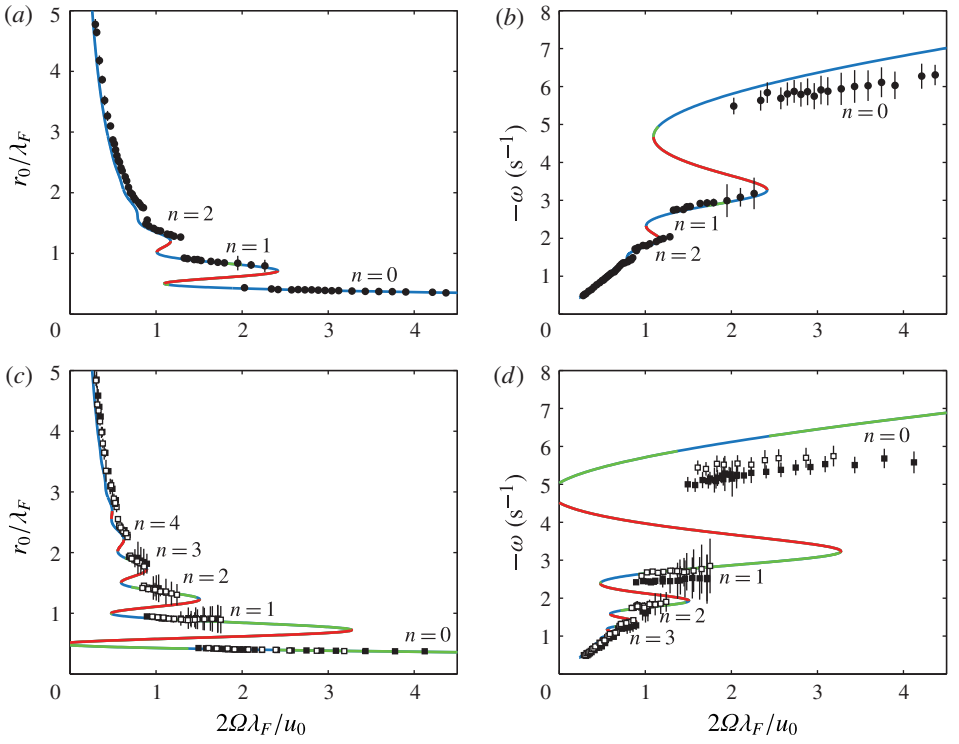

FIGURE 2. The predicted dependence of the orbital radius r_0 (*a*,*c*) and orbital frequency ω (*b*,*d*) on the bath's rotation rate Ω in the high-memory regime. The curves are the theoretical predictions determined by solving (4.1) with the experimental parameters corresponding to the data reported by Harris & Bush (2014), who used a silicone oil of viscosity $\nu = 20.9$ cSt, density $\rho = 950$ kg m^{-3}, surface tension $\sigma = 0.0206$ N m^{-1} and forcing frequency $f = 80$ Hz. There are no fitting parameters. The blue portions of the curves are stable, while the red and green portions are unstable (see § 5). For (*a*,*b*), $\gamma/\gamma_F = 0.954$, $R_D = 0.43$ mm and $u_0 = 12.0$ mm s^{-1}. For (*c*,*d*), $\gamma/\gamma_F = 0.971$, $R_D = 0.4$ mm and $u_0 = 10.9$ mm s^{-1} (■) and 11.7 mm s^{-1} (□). The theoretical curves in (*c*,*d*) are constructed using the average of the observed u_0 values. Note that both r_0 and ω are quantized.

As discussed in appendix A, this approximation is valid even for arbitrarily large $\hat{r}_0$. Both integrals in (4.2) can be evaluated exactly, yielding

$$-\kappa\hat{r}_0\hat{\omega}^2 - \hat{\Omega}\hat{r}_0\hat{\omega} = \frac{\beta\hat{r}_0\hat{\omega}^2}{2(1+(\hat{r}_0\hat{\omega})^2)^{3/2}}, \quad \hat{r}_0\hat{\omega} = \frac{\beta}{\hat{r}_0\hat{\omega}}\left(1 - \frac{1}{\sqrt{1+(\hat{r}_0\hat{\omega})^2}}\right). \tag{4.3}$$

The second equation allows us to solve for the orbital walking speed $\hat{u} \equiv |\hat{r}_0\hat{\omega}|$:

$$\hat{u} \equiv |\hat{r}_0\hat{\omega}| = \frac{1}{\sqrt{2}}\left(-1 + 2\beta - \sqrt{1+4\beta}\right)^{1/2}. \tag{4.4}$$

This is the same as the formula for the free speed $\hat{u}_0$ of a walker on a *non-rotating* bath (Oza *et al.* 2013), the non-dimensional equivalent of that given in table 1.

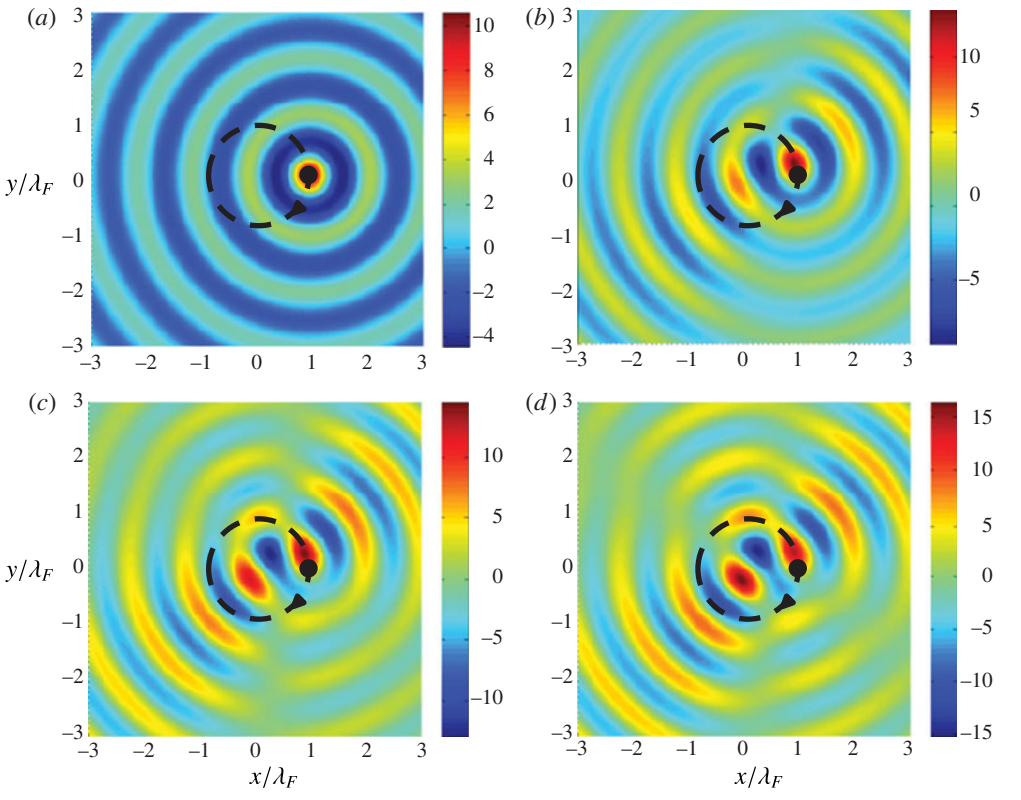

FIGURE 3. Plots of the wave field (3.2) accompanying a drop of viscosity $\nu = 20.9$ cSt, density $\rho = 950$ kg m^{-3}, surface tension $\sigma = 0.0206$ N m^{-1}, period $T_F = 0.025$ s, radius $R_D = 0.4$ mm and phase $\sin\Phi = 0.16$. The amplitude of the wave field is in units of micrometres. The drop (black dot) orbits clockwise according to $\boldsymbol{x}_p(t) = (r_0\cos\omega t, r_0\sin\omega t)$, with orbital radius $r_0 = 0.95\lambda_F$ and orbital frequency ω defined by (4.1). The forcing accelerations are (*a*) $\gamma/\gamma_F = 0.822$, (*b*) $\gamma/\gamma_F = 0.922$, (*c*) $\gamma/\gamma_F = 0.954$ and (*d*) $\gamma/\gamma_F = 0.971$. The walking threshold in the absence of rotation is $\gamma_W/\gamma_F = 0.806$. Note that interference effects in the wave field become more pronounced with increased forcing and path memory.

Substituting (4.4) into the first equation of (4.3) yields a formula for the orbital frequency $\hat{\omega}$:

$$\hat{\omega} = -\hat{\Omega}\left(\kappa + \frac{\beta}{2\left(1+\hat{u}_0^2\right)^{3/2}}\right)^{-1} = -\hat{\Omega}\left(\kappa + \frac{4\beta}{\left(-1+\sqrt{1+4\beta}\right)^3}\right)^{-1} \tag{4.5}$$

since $\sqrt{1+\hat{u}_0^2} = \frac{1}{2}(-1+\sqrt{1+4\beta})$. The solutions (4.4) and (4.5) are compatible with the initial assumption $|\hat{\omega}| \ll 1$ provided that $|\hat{\Omega}| \ll \kappa + 4\beta/(-1+\sqrt{1+4\beta})^3$.

In dimensional units, the orbital frequency ω and radius r_0 are given by

$$\omega = -\frac{2\Omega}{a}, \quad r_0 = \frac{au_0}{2\Omega}, \tag{4.6}$$

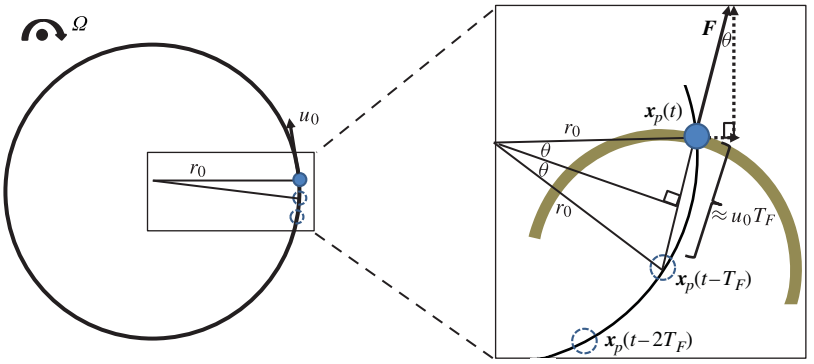

FIGURE 4. (Colour online) Schematic (top view) of the wave force acting on the walker in the low-memory regime. The walker orbits in a circle of radius r_0 with angular speed $u_0 = |r_0\omega|$ while bouncing with period T_F on a fluid bath rotating with angular frequency Ω. The force $\boldsymbol{F}$ acting on the drop at $\boldsymbol{x} = \boldsymbol{x}_p(t)$ is primarily due to the wave created by the prior bounce at $\boldsymbol{x} = \boldsymbol{x}_p(t - T_F)$, whose form is suggested by the circular wave crest. The radial component of the force is $|\boldsymbol{F}| \sin\theta$. The wave force thus causes the observed orbital radius $r_0 = au_0/2\Omega$ to be larger than the inertial orbital radius $r_c = u_0/2\Omega$.

where

$$a = 1 + \frac{4\beta}{\kappa\left(-1+\sqrt{1+4\beta}\right)^3} = 1 + \frac{4FM_e^3T_F^2k_F}{m\left(-1+\sqrt{1+4FM_e^2T_Fk_F/D}\right)^3}. \tag{4.7}$$

Over the parameter regime explored in the experiments of Harris & Bush (2014), a was measured to be 1.51, and calculated using (4.7) to be 1.41. Both results are consistent with the empirical deduction of $a = 1.2$–1.5 reported by Fort *et al.* (2010). Plots of the drop's orbital radius and orbital frequency as a function of Ω in the low-memory regime are shown in figure 1(*a*,*b*), and adequately collapse the data presented in Harris & Bush (2014). In figure 1(*c*,*d*), we begin to see some deviation from the low-memory result (4.6) for the orbits of smallest radius, as these orbits have the longest orbital memory.

The a-factor, and the associated increase of the orbital radius relative to inertial orbits, may be understood in terms of the geometry of the wave force. Figure 4 shows that the force $\boldsymbol{F}$ on the drop due to the wave generated during its prior impact has a component $|\boldsymbol{F}| \sin\theta = |\boldsymbol{F}|\, u_0T_F/2r_0$ that points radially outwards. In the low-orbital-memory regime, the drop's trajectory is primarily influenced by the waves generated by a few prior impacts, all of which make contributions pointing radially outwards. The prefactor a can thus be understood as originating from the dynamic influence of the walker's guiding wavefield. Alternatively, the anomalously large radius of the walker's orbit may be understood as resulting from an increased effective mass $\tilde{m}$ associated with its wave field, as (4.3) may be expressed in dimensional form as

$$\frac{\tilde{m}u_0^2}{r_0} = 2m\Omega u_0, \quad \text{where } \frac{\tilde{m}}{m} = a. \tag{4.8}$$

4.2. *Mid-memory $M_e^O = O(1)$: orbital quantization*

In the low-orbital-memory regime $M_e^O \ll 1$, the drop's orbital radius r_0 is a monotonically decreasing function of the rotation rate Ω, as shown in figure 1.

Solving the algebraic equations (4.1) numerically indicates that such is no longer the case in the mid-orbital-memory regime $M_e^O = O(1)$, which arises at higher forcing acceleration γ/γ_F. The solution curve first develops an inflection point and then two turning points. More turning points appear with increasing memory M_e, as shown in figure 2(*a*,*c*). In § 5, we will show that the regions of the solution curves with positive slope represent unstable orbital solutions. The unstable regions of the solution curve represent forbidden orbital radii. This demonstrates the origins of orbital quantization: the set of observable orbital radii is discrete and discontinuous. This system represents a classical analogue of the quantized Landau levels of an electron in a uniform magnetic field (Fort *et al.* 2010). Here, however, the walker's orbital quantization can be rationalized in terms of its pilot-wave dynamics.

We follow the convention of Fort *et al.* (2010) for numbering the orbits, the smallest being denoted by $n = 0$. At certain rotation rates, orbital degeneracy arises: multiple orbits of different radii may exist for a fixed rotation rate. The orbital degeneracy becomes even more pronounced at high memory, as we observe the coexistence of up to three possible radii for a single rotation rate. Even at the highest path memory considered, as the orbits become larger in radius, they cease to be quantized, and the data essentially follows the low-memory curve. This might be anticipated on the grounds that, for sufficiently large radii, the drop is in the low-orbital-memory regime $M_e^O \ll 1$: its orbital period $T_O \approx 2\pi r_0/u_0$ is much longer than the decay time $T_F M_e$ of its wave field.

The equations in (4.1) adequately capture the observed dependence of the orbital radius r_0 and frequency ω on Ω and M_e. Note that, in figure 2(*b*,*d*), the largest discrepancy between theory and experiment occurs in frequencies ω of the innermost orbital $n = 0$, for which $r_0/\lambda_F < 0.5$. Such a discrepancy might be accounted for through a variation of the bouncing phase $\sin\Phi$ for the smallest orbits.

4.3. *High orbital memory $M_e^O \gg 1$: an analogue Zeeman effect*

The set of orbital solutions has qualitatively different behaviour in the high-orbital-memory limit $M_e^O \gg 1$, or equivalently $|\hat{\omega}| \gg 1$. Let Ω be the rotation rate of the container, in which the drop orbits with radius r_0 and orbital frequency ω. If the container rotates in the opposite direction (with angular frequency $-\Omega$), the drop will clearly orbit with the same radius r_0 but opposite orbital frequency $-\omega$. Thus, the solution curves for the orbital radii in figures 1 and 2 should be symmetric about the vertical axis, with an additional curve corresponding to solutions with identical radii for $\Omega < 0$. As the memory M_e increases, the solution curves approach the r_0-axis and, in the high-memory limit, eventually cross, as shown in figure 5(*a*). Our pilot-wave model thus predicts the possibility of a *self-orbiting solution* with some radius r_0^* that exists even in the absence of rotation, at $\Omega = 0$. For such solutions, which might be interpreted as 'hydrodynamic spin states', the waves generated by the walker are sufficient to compensate for the absent Coriolis force, balancing the radial inertial force and so sustaining the walker's circular motion.

Note that the self-orbiting solutions (arising at $\Omega = 0$) come in pairs, corresponding to positive and negative angular frequencies $\pm\omega^*$ (figure 5*c*). As shown in figure 5(*b*), the introduction of a finite rotation $\Omega > 0$ causes these two degenerate solutions to split, one with radius $r_0 \gtrsim r_0^*$ and the other with $r_0 \lesssim r_0^*$. To see this explicitly, we seek solutions to (4.1) with high orbital memory $|\hat{\omega}| \gg 1$, which only arise in the high-path-memory regime $M_e \gg 1$. Specifically, we take $\beta \gg 1$, $\kappa = O\big(\beta^{-1/2}\big)$, $\hat{\omega} = O\big(\beta^{1/2}\big)$, $\hat{\Omega} = O(1)$ and $\hat{r}_0 = O(1)$. We first use integration by parts to rewrite the

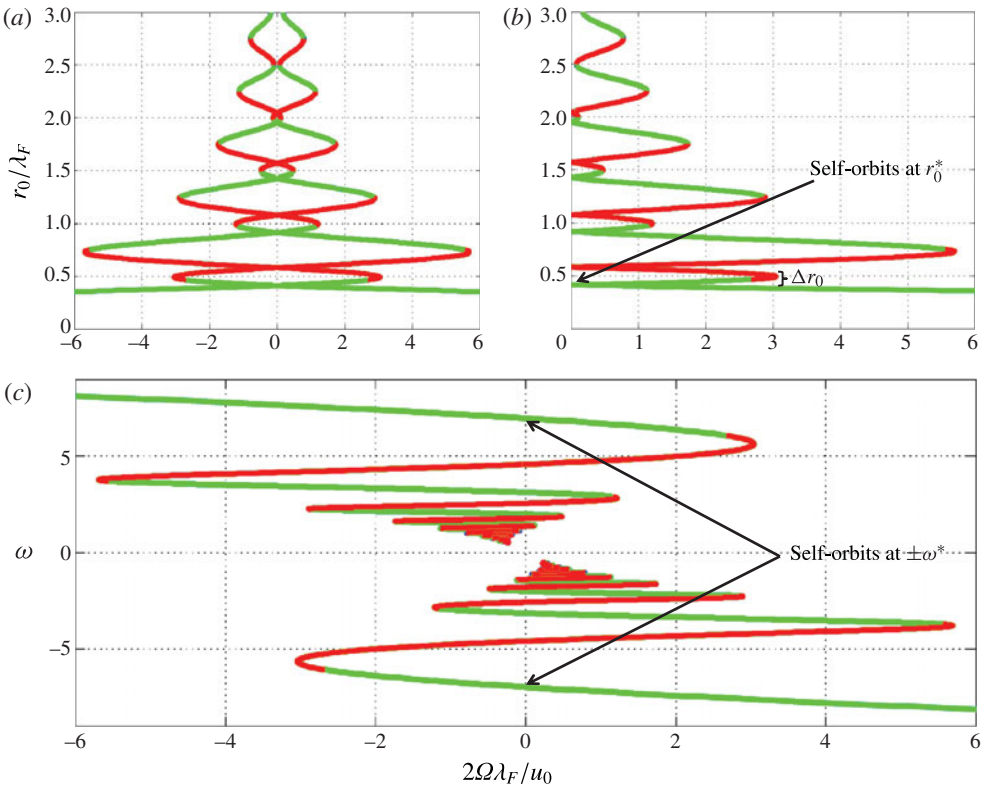

FIGURE 5. Orbital solutions in the high-orbital-memory regime $M_e^O \gg 1$. The curves are determined by solving (4.1) numerically for $\gamma/\gamma_F = 0.985$, assuming a drop of radius $R_D = 0.4$ mm, phase $\sin\Phi = 0.16$ and free walking speed $u_0 = 11.6$ mm s^{-1}. Both the red and green portions of the curves represent unstable solutions (see § 5). (*a*) Orbital radii as a function of Ω. (*b*) Orbital radii for which $\Omega > 0$. (*c*) Orbital frequencies ω as a function of Ω. The analogue Zeeman effect is apparent in (*b*), as the self-orbiting solutions of radius r_0^* at $\Omega = 0$ split into two solutions as Ω is increased. The adjoining co-rotating orbital solutions ($\omega > 0$) have slightly larger orbital radii than their counter-rotating counterparts ($\omega < 0$), the difference Δr_0 being defined in (4.17).

second equation in (4.1) in the form

$$\hat{r}_0\hat{\omega} = \frac{\beta}{\hat{r}_0\hat{\omega}}\left[1 - \int_0^\infty J_0\left(2\hat{r}_0 \sin\frac{\hat{\omega}z}{2}\right)\mathrm{e}^{-z}\,\mathrm{d}z\right]. \tag{4.9}$$

For a 2π-periodic even function $f(x)$ and $0 < \epsilon \ll 1$, we have the approximation

$$\epsilon\int_0^\infty f(x)\mathrm{e}^{-\epsilon x}\,\mathrm{d}x = \frac{\epsilon}{1-\mathrm{e}^{-2\pi\epsilon}}\int_0^{2\pi} f(x)\mathrm{e}^{-\epsilon x}\,\mathrm{d}x = \frac{1}{2\pi}\int_0^{2\pi} f(x)\,\mathrm{d}x + O(\epsilon^2), \tag{4.10}$$

from which it follows that

$$\int_0^\infty J_1\left(2\hat{r}_0\sin\frac{\hat{\omega}z}{2}\right)\sin\frac{\hat{\omega}z}{2}\mathrm{e}^{-z}\,\mathrm{d}z = \frac{1}{2\pi}\int_0^{2\pi} J_1\left(2\hat{r}_0\sin x\right)\sin x\,\mathrm{d}x + O\left(\hat{\omega}^{-2}\right), \tag{4.11a}$$

$$\int_0^\infty J_0\left(2\hat{r}_0\sin\frac{\hat{\omega}z}{2}\right)\mathrm{e}^{-z}\,\mathrm{d}z = \frac{1}{2\pi}\int_0^{2\pi} J_0\left(2\hat{r}_0\sin x\right)\,\mathrm{d}x + O\left(\hat{\omega}^{-2}\right). \tag{4.11b}$$

We simplify these integrals by using the identity (Watson 1966, p. 151)

$$\int_0^{\pi/2} J_{p-q}\,(a\cos x)\cos(p+q)x\,\mathrm{d}x = \frac{\pi}{2}(-1)^q J_p(a/2)J_q(a/2), \quad p,\,q \text{ integers} \tag{4.12}$$

which implies that

$$\int_0^{\pi/2} J_1(a\cos x)\cos x\,\mathrm{d}x = \frac{\pi}{2}J_0(a/2)J_1(a/2), \quad (p=1,\,q=0), \tag{4.13a}$$

$$\int_0^{\pi/2} J_0(a\cos x)\cos x\,\mathrm{d}x = \frac{\pi}{2}J_0^2(a/2), \quad (p=0,\,q=0). \tag{4.13b}$$

Letting $x \to x+\pi/2$, we find that

$$\frac{1}{2\pi}\int_0^{2\pi} J_1(a\sin x)\sin x\,\mathrm{d}x = J_0(a/2)J_1(a/2), \quad \frac{1}{2\pi}\int_0^{2\pi} J_0(a\sin x)\,\mathrm{d}x = J_0^2(a/2), \tag{4.14}$$

and thus obtain the high-orbital-memory limit of (4.1):

$$\left.\begin{aligned} -\kappa\hat{r}_0\hat{\omega}^2 &= \beta\left[J_0(\hat{r}_0)J_1(\hat{r}_0) + O\left(\hat{\omega}^{-2}\right)\right] + \hat{\Omega}\hat{r}_0\hat{\omega} \\ \hat{r}_0\hat{\omega} &= \frac{\beta}{\hat{r}_0\hat{\omega}}\left[1 - J_0(\hat{r}_0)^2 + O\left(\hat{\omega}^{-2}\right)\right]. \end{aligned}\right\} \tag{4.15}$$

Let $\hat{r}_0^*$ be a zero of either $J_0(r)$ or $J_1(r)$. To leading order in β, the orbital radius $\hat{r}_0$ and frequency $\hat{\omega}$ are

$$\begin{aligned} \hat{r}_0 &= \hat{r}_0^* + \frac{\kappa\hat{r}_0^*\hat{\omega}^{*2}}{\beta}\left(1 + \frac{\hat{\Omega}}{\kappa\hat{\omega}^*}\right) \\ &\quad \times \begin{cases} J_1(\hat{r}_0^*)^{-2}, & \text{if } J_0(\hat{r}_0^*) = 0 \\ -\left[J_0(\hat{r}_0^*)J_1'(\hat{r}_0^*)\right]^{-1}, & \text{if } J_1(\hat{r}_0^*) = 0. \end{cases} + O\left(\beta^{-1}\right), \end{aligned} \tag{4.16a}$$

$$\hat{\omega}^* = \left(\frac{\beta\left(1 - J_0(\hat{r}_0^*)^2\right)}{\hat{r}_0^{*2}}\right)^{1/2} + O(1). \tag{4.16b}$$

The radii $\hat{r}_0$ satisfying $J_1(\hat{r}_0) \approx 0$ correspond to solutions in the red portions of the curve and are never observed experimentally, as is evident in figure 2(*c*), so we instead consider the solutions with $J_0(\hat{r}_0) \approx 0$. We note that these solutions, although also unstable, do leave an imprint on the walker's statistics in the high-memory limit (Harris & Bush 2014; Oza *et al.* 2014*b*). Taking $\hat{\Omega} > 0$, we see from (4.16) that co-rotating solutions ($\hat{\omega} > 0$) have slightly larger radii than the counter-rotating solutions ($\hat{\omega} < 0$). In terms of dimensional variables, the difference in radius Δr_0 is prescribed by

$$\frac{\Delta r_0}{\lambda_F} = \frac{2mr_0^*\,|\omega^*|}{FM_e\pi J_1(k_F r_0^*)^2}\Omega, \quad \text{where } r_0^* \text{ is defined by } J_0(k_F r_0^*) = 0. \tag{4.17}$$

Thus, the magnitude of the splitting is proportional to the rotation rate Ω. Building upon the correspondence proposed by Fort *et al.* (2010) between inertial orbits and Landau levels, we see that this orbital splitting represents a hydrodynamic analogue of the Zeeman effect, in which an electron's degenerate energy level splits in the presence of a uniform magnetic field. For weak fields, the size of the split

is proportional to the strength of the magnetic field. We note that this splitting is similar in form to that reported by Eddi *et al.* (2012) for orbiting pairs of walkers in a rotating frame, but would apply to single orbiting walkers were such hydrodynamic spin states stable.

We observe from (4.16*a*) that, in the high-orbital-memory regime, the physically significant orbital radii may be approximated by the zeros of the Bessel function $J_0(k_F r)$. We note that the approximation (2.3) proposed by Fort *et al.* (2010) is consistent with this result for large r_0. Indeed, using the approximation $J_\alpha(x) \approx \sqrt{2/\pi x}\cos(x - \alpha\pi/2 - \pi/4)$ for $x \gg |\alpha^2 - 1/4|$, the radial equation in (4.15) for counter-rotating solutions ($\omega < 0$) can be expressed as

$$\frac{mu^2}{r_0} \approx 2m\Omega u + \frac{FM_e}{\pi k_F r_0}\cos(2k_F r_0), \quad \text{where } u = r_0|\omega|. \tag{4.18}$$

This is similar in form to the high-memory governing equation (2.2) proposed by Fort *et al.* (2010), which was derived using purely geometrical arguments. Both equations indicate that most of the sources on the circle cancel out, and that the droplet essentially orbits in the wave field created by a virtual droplet of mass $\tilde{m} = mM_e/\pi k_F r_0$ on the opposite side of the circle. However, we expect (4.18) to be valid only for sufficiently large orbital radii r_0, for which the large-argument approximation for $J_\alpha(x)$ may be safely applied.

4.4. *Trapped states*

We now consider orbits of small radius, specifically $r_0 \ll \lambda_F/2$. In the limit of $r_0 \to 0$, the non-dimensional equations (4.1) reduce to

$$-\kappa\hat{\omega}_0^2 - \hat{\Omega}_0\hat{\omega}_0 = \beta\int_0^\infty \sin^2\frac{\hat{\omega}_0 z}{2}\mathrm{e}^{-z}\,\mathrm{d}z, \quad \hat{\omega}_0 = \frac{\beta}{2}\int_0^\infty \sin\hat{\omega}_0 z\,\mathrm{e}^{-z}\,\mathrm{d}z \tag{4.19}$$

where $\hat{\omega}_0$, $\hat{\Omega}_0$ are the values corresponding to the $\hat{r}_0 = 0$ solution. The integrals can be evaluated explicitly, which yields the system of equations

$$\kappa\hat{\omega}_0^2 + \hat{\Omega}_0\hat{\omega}_0 = -\frac{\beta\hat{\omega}_0^2}{2\left(1+\hat{\omega}_0^2\right)}, \quad \hat{\omega}_0 = \frac{\beta\hat{\omega}_0}{2\left(1+\hat{\omega}_0^2\right)} \tag{4.20}$$

with solutions

$$\hat{\omega}_0 = \pm\sqrt{\frac{\beta}{2} - 1}, \quad \hat{\Omega}_0 = -\hat{\omega}_0(1+\kappa). \tag{4.21}$$

We call these solutions *trapped states*, as they have infinitesimal radius but finite orbital frequency. In terms of dimensional variables, the angular frequencies ω_0 and Ω_0 corresponding to these trapped states are

$$\omega_0 = \frac{1}{T_F M_e}\sqrt{\frac{Fk_F T_F M_e^2}{2D} - 1}, \quad \Omega_0 = \frac{D}{2m}\sqrt{\frac{Fk_F T_F M_e^2}{2D} - 1}\left(1 + \frac{m}{DM_e T_F}\right). \tag{4.22}$$

It is shown in Oza, Bush & Rosales (2014*a*) that the bouncing state $\boldsymbol{x}_p \equiv$ constant is stable for $|\Omega| > \Omega_0$. That is, even above the walking threshold ($\gamma > \gamma_W$), the drop will simply bounce in place if the rotation rate is sufficiently high ($|\Omega| > \Omega_0$). The stability of the bouncing state is determined by the balance between the destabilizing

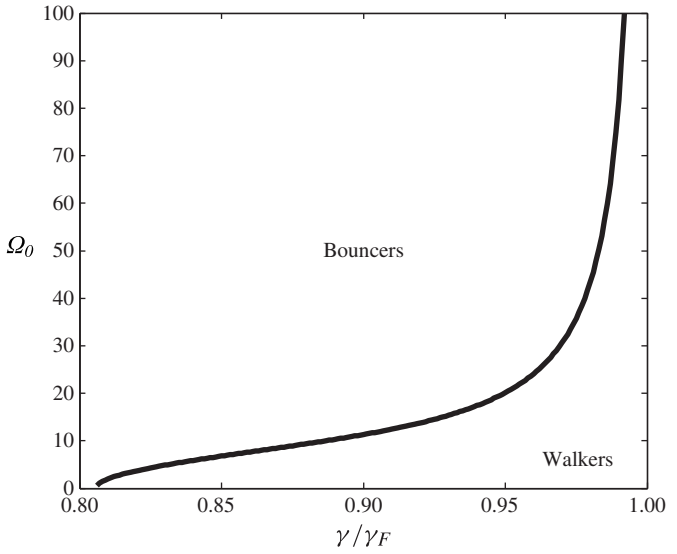

FIGURE 6. The critical rotation rate for trapping Ω_0 as defined by (4.22) is plotted as a function of the non-dimensional forcing acceleration γ/γ_F. The drop bounces in place for $|\Omega| > \Omega_0$ (Oza *et al.* 2014*a*). We assume a drop of radius $R_D = 0.4$ mm and phase $\sin\Phi = 0.16$, for which the walking threshold in the absence of rotation is $\gamma_W/\gamma_F = 0.806$.

wave force and the stabilizing effects of the drag force (which opposes the drop's motion) and the Coriolis force (which radially confines the drop).

Figure 6 shows that the critical rotation rate required for trapping, Ω_0, is an increasing function of the forcing acceleration γ, and diverges as $\gamma \to \gamma_F$. Experimental validation of the curve presented in figure 6 was impractical owing to the significant deflection of the free surface at high Ω, which caused the Faraday threshold to be spatially non-uniform. Thus, the prediction (4.22) for the critical rotation rate Ω_0 could not be tested reliably with our experimental arrangement.

5. Orbital stability

In order to rationalize the observed orbital quantization, we proceed by analysing the stability of the orbital solutions found in § 4. To this end, we write $\boldsymbol{x}_p(t) = (r(t)\cos\theta(t), r(t)\sin\theta(t))$ and express the non-dimensional equation of motion (3.4) in polar coordinates, all of the variables here being non-dimensional. We thus obtain

$$\begin{aligned}\kappa\left(\ddot{r} - r\dot{\theta}^2\right) + \dot{r} &= \beta\int_{-\infty}^{t}\frac{J_1(|\boldsymbol{x}_p(t)-\boldsymbol{x}_p(s)|)}{|\boldsymbol{x}_p(t)-\boldsymbol{x}_p(s)|}\\ &\quad\times\left[r(t)-r(s)\cos\left(\theta(t)-\theta(s)\right)\right]\mathrm{e}^{-(t-s)}\,\mathrm{d}s\\ &\quad+\Omega r\dot{\theta}+\epsilon c_r\delta(t) \qquad (5.1a)\\ \kappa\left(2\dot{r}\dot{\theta}+r\ddot{\theta}\right)+r\dot{\theta} &= \beta\int_{-\infty}^{t}\frac{J_1(|\boldsymbol{x}_p(t)-\boldsymbol{x}_p(s)|)}{|\boldsymbol{x}_p(t)-\boldsymbol{x}_p(s)|}\\ &\quad\times r(s)\sin\left(\theta(t)-\theta(s)\right)\mathrm{e}^{-(t-s)}\,\mathrm{d}s\\ &\quad-\Omega\dot{r}+\epsilon r_0 c_\theta\delta(t), \qquad (5.1b)\end{aligned}$$

where

$$\left|\boldsymbol{x}_p(t)-\boldsymbol{x}_p(s)\right|^2 = r(t)^2 + r(s)^2 - 2r(t)r(s)\cos\left(\theta(t)-\theta(s)\right), \tag{5.2}$$

and $\delta_r(t)$, $\delta_\theta(t)$ are Dirac delta functions, c_r, c_θ are $O(1)$ constants and $0<\epsilon\ll 1$. The delta functions represent a small perturbation to the drop at time $t=0$, the response to which we examine in what follows.

We linearize (5.1) about an orbital solution of radius r_0 and frequency ω, where r_0 and ω are defined by (4.1). The drop's trajectory is thus written as $r(t) = r_0 + \epsilon r_1(t)H(t)$ and $\theta(t) = \omega t + \epsilon\theta_1(t)H(t)$, where $r_1(t)$ and $\theta_1(t)$ are the radial and angular perturbations to the orbital solution, respectively, and $H(t)$ is the Heaviside step function. We impose the conditions $r_1(0)=\theta_1(0)=0$ and $\dot{r}_1(0)=c_r/\kappa$, $\dot{\theta}_1(0)=c_\theta/\kappa$ in order to ensure that $\boldsymbol{x}_p(t)$ is a solution of (5.1). We substitute these expressions into (5.1) and retain only the $O(\epsilon)$ terms to find

$$\begin{aligned}\kappa\left(\ddot{r}_1-\omega^2 r_1-2r_0\omega\dot{\theta}_1\right)+\dot{r}_1 &= \omega\Omega r_1+\Omega r_0\dot{\theta}_1+\frac{\beta}{2}\left\{\mathscr{I}\left[\left(f(t)+g(t)\right)\sin\omega t\right]r_0\theta_1(t)\right.\\ &\left.-r_0\left[\left(f(t)+g(t)\right)\sin\omega t\right]*\theta_1(t)\right\}+\beta\left\{\mathscr{I}\left[f(t)\cos^2\frac{\omega t}{2}+g(t)\sin^2\frac{\omega t}{2}\right]r_1(t)\right.\\ &\left.+\left(g(t)\sin^2\frac{\omega t}{2}-f(t)\cos^2\frac{\omega t}{2}\right)*r_1(t)\right\} \qquad (5.3a)\end{aligned}$$

$$\begin{aligned}\kappa\left(2\omega\dot{r}_1+r_0\ddot{\theta}_1\right)+\omega r_1+r_0\dot{\theta}_1 &= -\Omega\dot{r}_1+\frac{\beta}{2}\left\{\mathscr{I}\left[\left(g(t)-f(t)\right)\sin\omega t\right]r_1(t)\right.\\ &\left.+\left[\left(f(t)+g(t)\right)\sin\omega t\right]*r_1(t)\right\}+\beta\left\{\mathscr{I}\left[g(t)\cos^2\frac{\omega t}{2}-f(t)\sin^2\frac{\omega t}{2}\right]r_0\theta_1(t)\right.\\ &\left.+r_0\left(f(t)\sin^2\frac{\omega t}{2}-g(t)\cos^2\frac{\omega t}{2}\right)*\theta_1(t)\right\} \qquad (5.3b)\end{aligned}$$

where

$$\left.\begin{aligned} f(z) &= \frac{J_1(2r_0\sin(\omega z/2))}{2r_0\sin(\omega z/2)}\mathrm{e}^{-z}, \quad g(z) = J_1'\left(2r_0\sin\frac{\omega z}{2}\right)\mathrm{e}^{-z},\\ \mathscr{I}[f] &= \int_0^\infty f(z)\,\mathrm{d}z \quad \text{and} \quad f*g(t) = \int_0^t f(z)g(t-z)\,\mathrm{d}z.\end{aligned}\right\} \tag{5.4}$$

Written in this form, the linearized equations are particularly amenable to analysis, as we can now take their Laplace transform and deduce algebraic equations for $R(s)=\mathscr{L}[r_1]$ and $\Theta(s)=\mathscr{L}[\theta_1]$. Using the initial conditions $r_1(0)=\theta_1(0)=0$ and $\dot{r}_1(0)=c_r/\kappa$, $\dot{\theta}_1(0)=c_\theta/\kappa$, we obtain

$$\left.\begin{aligned}\left[\kappa s^2+s-\kappa\omega^2-\Omega\omega-\beta F_1(s)\right]R-\left[2\kappa\omega s+\Omega\omega s+\beta F_2(s)\right]r_0\Theta &= c_r\\ \left[2\omega\kappa s+\omega+\Omega s-\beta G_1(s)\right]R+\left[\kappa s^2+s-\beta G_2(s)\right]r_0\Theta &= r_0c_\theta,\end{aligned}\right\} \tag{5.5}$$

where

$$F_1(s) = \mathscr{I}\left[f(t)\cos^2\frac{\omega t}{2}+g(t)\sin^2\frac{\omega t}{2}\right]+\mathscr{L}\left[g(t)\sin^2\frac{\omega t}{2}-f(t)\cos^2\frac{\omega t}{2}\right] \tag{5.6a}$$

$$F_2(s) = \frac{1}{2}\left\{\mathscr{I}\left[\left(f(t)+g(t)\right)\sin\omega t\right]-\mathscr{L}\left[\left(f(t)+g(t)\right)\sin\omega t\right]\right\} \tag{5.6b}$$

$$G_1(s) = \frac{1}{2}\left\{\mathscr{I}\left[\left(g(t)-f(t)\right)\sin\omega t\right]+\mathscr{L}\left[\left(f(t)+g(t)\right)\sin\omega t\right]\right\} \tag{5.6c}$$

$$G_2(s) = \mathscr{I}\left[g(t)\cos^2\frac{\omega t}{2}-f(t)\sin^2\frac{\omega t}{2}\right]+\mathscr{L}\left[f(t)\sin^2\frac{\omega t}{2}-g(t)\cos^2\frac{\omega t}{2}\right]. \tag{5.6d}$$

As shown in appendix B, some of the integrals above can be done in closed form, so (5.5) can be expressed as

$$\begin{bmatrix} A(s) & -B(s) \\ C(s) & D(s) \end{bmatrix} \begin{bmatrix} R(s) \\ r_0\Theta(s) \end{bmatrix} = \begin{bmatrix} c_r \\ r_0 c_\theta \end{bmatrix} \tag{5.7}$$

where

$$A(s) = \kappa s^2 + s - \kappa\omega^2 - \Omega\omega - \beta\left(\mathscr{I}\left[f(t)\cos^2\frac{\omega t}{2} + g(t)\sin^2\frac{\omega t}{2}\right] + \mathscr{L}\left[g(t)\sin^2\frac{\omega t}{2} - f(t)\cos^2\frac{\omega t}{2}\right]\right) \tag{5.8a}$$

$$B(s) = (2\omega\kappa + \Omega)\, s - (\kappa\omega + \Omega) - \frac{\beta}{2}\mathscr{L}\left[(f(t) + g(t))\sin\omega t\right] \tag{5.8b}$$

$$C(s) = (2\omega\kappa + \Omega)\, s + 2\omega + \kappa\omega + \Omega - \frac{\beta}{2}\mathscr{L}\left[(f(t) + g(t))\sin\omega t\right] \tag{5.8c}$$

$$D(s) = \kappa s^2 + s - 1 - \beta\mathscr{L}\left[f(t)\sin^2\frac{\omega t}{2} - g(t)\cos^2\frac{\omega t}{2}\right]. \tag{5.8d}$$

The solution to (5.7) is

$$R(s) = \frac{c_r D(s) + r_0 c_\theta B(s)}{A(s)D(s) + B(s)C(s)} \tag{5.9a}$$

$$\Theta(s) = \frac{-c_r C(s) + r_0 c_\theta A(s)}{r_0\,(A(s)D(s) + B(s)C(s))}. \tag{5.9b}$$

The poles of $R(s)$ and $\Theta(s)$ are the eigenvalues of the linear problem (5.3). If all of the poles lie in the left-half complex plane, the orbital solution $\boldsymbol{x}_p(t) = (r_0\cos\omega t,\, r_0\sin\omega t)$ is linearly stable. An instability occurs if any pole is in the right-half complex plane.

It is shown in Oza *et al.* (2014*a*) that a necessary and sufficient condition for either $R(s)$ or $\Theta(s)$ to have a pole at $s = s^*$ is $\tilde{F}(s^*;\, r_0) = 0$, where

$$\tilde{F}(s;\, r_0) = \left(1 - \mathrm{e}^{2\pi(s+1)/|\omega|}\right) F(s;\, r_0), \quad F(s;\, r_0) = A(s)D(s) + B(s)C(s). \tag{5.10}$$

Thus, assessing the stability of an orbital solution with radius r_0 amounts to finding the real parts of the zeros of the function $\tilde{F}(s;\, r_0)$. Note that we parametrize the orbital solutions in terms of the radius r_0 instead of the non-dimensional rotation rate Ω, since ω and Ω are single-valued functions of r_0. That is, the radius r_0 uniquely determines the drop's orbital frequency ω and the bath rotation rate Ω, but multiple radii r_0 could exist for a given value of Ω, as predicted by (4.1) and seen in experiments (figure 2; see also Harris & Bush (2014) and Fort *et al.* (2010)).

It is shown in Oza *et al.* (2014*a*) that $\tilde{F}(s;\, r_0)$ has trivial zeros at $s = 0$ and $s = \pm\mathrm{i}\omega$, which reflect, respectively, the rotational and translational invariance of the orbital solution. Note that $\tilde{F}(s;\, r_0)$ is a complicated function of s, so it is difficult to determine its nontrivial zeros in closed form. In Oza *et al.* (2014*a*), we instead expand $\tilde{F}(s;\, r_0)$ in various limits for which we can approximate its zeros and thus assess the stability of the orbital solutions in the appropriate parameter regimes. We show that orbits of small radius $r_0 \ll 1$ are stable, which confirms that the bouncing state destabilizes into an orbital state with radius $r_0 \sim |\Omega_0 - \Omega|^{1/2}$ for $\Omega \lesssim \Omega_0$. We

also show that the stability problem for orbits of large radius $r_0 \gg \sqrt{\beta}$ reduces to that for steady rectilinear walking; this is apparent on physical grounds, as such orbits have small curvature and so can be approximated locally by a straight line. Since steady rectilinear walking is stable (Oza *et al.* 2013), we expect that such large orbits will be likewise, which is consistent with our inference that such orbits are not quantized (figures 1 and 2).

5.1. *Origin of orbital quantization*

Here we demonstrate that the orbital solutions for which $\mathrm{d}\Omega/\mathrm{d}r_0 > 0$ are unstable. This explains why the upward sloping branches of the solution curves in figure 2(*a*,*c*) are never seen experimentally, a feature that is ultimately responsible for the orbital quantization.

We proceed by proving the following result.

THEOREM 1. *Orbital solutions for which* $\mathrm{d}\Omega/\mathrm{d}r_0 > 0$ *are linearly unstable, with an instability corresponding to a real and positive eigenvalue.*

Proof. Let $F(s;\, r_0) = F_0(r_0)s + F_1(r_0)s^2 + O(s^3)$. We show in appendix C that $F_0(r_0) = r_0\omega d_1(\mathrm{d}\Omega/\mathrm{d}r_0)$, where $d_1 = 1 + \beta\mathscr{I}\left[\left(f(t)\sin^2(\omega t/2) - g(t)\cos^2(\omega t/2)\right)t\right]$. Since $F(s;\, r_0) \sim \kappa^2 s^4$ as $s \to \infty$, it follows that $F(s;\, r_0)$ has at least one positive real root if $F_0(r_0) < 0$. Since $d_1 > 0$ (Oza *et al.* 2014*a*) and $\omega < 0$, $F_0(r_0)$ has the opposite sign as $\mathrm{d}\Omega/\mathrm{d}r_0$. It follows that $F(s;\, r_0)$ has at least one real positive root if $\mathrm{d}\Omega/\mathrm{d}r_0 > 0$. □

Figure 7 summarizes the stability characteristics of the circular orbits. For a given value of the dimensionless forcing acceleration γ/γ_F, the stability of an orbital solution of radius r_0 is assessed by finding the zeros of $\tilde{F}(s;\, r_0)$, using the method detailed in Oza *et al.* (2014*a*). The perturbations $r_1(t)$ and $\theta_1(t)$ to the orbital solution will behave like $\mathrm{e}^{s_* t}$, where s_* is the zero of $\tilde{F}(s;\, r_0)$ with the largest real part. The points coloured in blue signify stable orbits, for which all of the zeros lie in the left-half of the complex plane ($\mathrm{Re}(s_*) < 0$). The points coloured in red and green signify unstable orbits ($\mathrm{Re}(s_*) > 0$). Unstable orbits for which s_* has a non-zero imaginary component ($\mathrm{Re}(s_*) > 0$, $\mathrm{Im}(s_*) \neq 0$) are coloured green, while those for which s_* is on the positive real axis ($\mathrm{Re}(s_*) > 0$, $\mathrm{Im}(s_*) = 0$) are coloured red.

We find that orbits for which $\mathrm{d}\Omega/\mathrm{d}r_0 > 0$, proven to be unstable in Theorem 1, are contained within the red regions of figure 7. We note that the converse of Theorem 1 is not necessarily true: orbital solutions for which $\mathrm{d}\Omega/\mathrm{d}r_0 < 0$ are not necessarily stable, as indicated by the green regions in figure 2(*a*,*c*). While orbital solutions are observed within these green regions, their relatively large error bars reflect a periodic fluctuation in the measured radius of curvature, corresponding to a wobbling orbit (Harris & Bush 2014). We may thus surmise that the oscillatory instability is stabilized by a nonlinear mechanism beyond the scope of our linear stability analysis.

Figure 7 indicates that all circular orbits are stable for $\gamma/\gamma_F < 0.930$. Above this critical value, an unstable (red) solution branch arises for $r_0 \approx 0.6\lambda_F$, corresponding roughly to the first positive zero of $J_1(k_F r)$. Along horizontal traverse B, there are two unstable branches, which correspond to the red portions of the curve in figure 2(*a*). As γ/γ_F is progressively increased, more unstable red tongues arise, for increasing orbital radius. The orbital solutions have blue, red and green branches along traverse C ($\gamma/\gamma_F = 0.971$), corresponding to the curve presented in figure 2(*c*). We note that

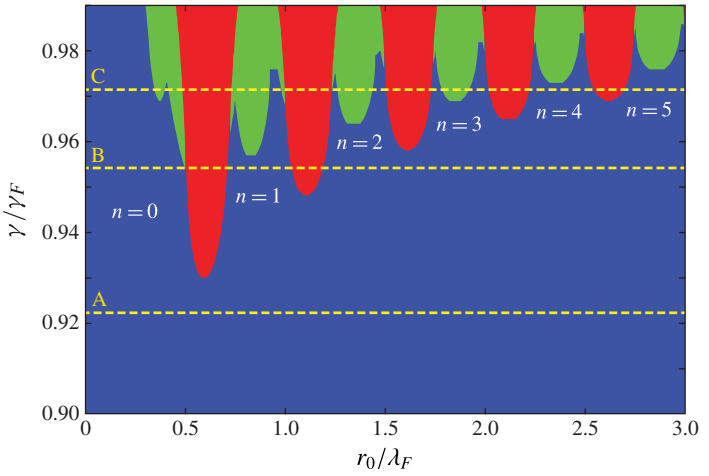

FIGURE 7. Orbital stability diagram for a walker of radius $R_D = 0.4$ mm, phase $\sin\Phi = 0.16$, viscosity $\nu = 20.9$ cSt, and forcing frequency $f = 80$ Hz, determined by finding the eigenvalues of the linear stability problem (5.3). The stability of the circular orbit is governed by the eigenvalue with the largest real part, denoted by s_*. Stable orbits ($\mathrm{Re}(s_*) < 0$) are indicated in blue. Unstable orbits for which s_* is complex ($\mathrm{Re}(s_*) > 0$, $\mathrm{Im}(s_*) \neq 0$) are coloured in green, while those for which s_* is on the positive real axis ($\mathrm{Re}(s_*) > 0$, $\mathrm{Im}(s_*) = 0$) are coloured in red. The horizontal traverses A–C correspond to, respectively, the curves in figures 1(*c*), 2(*a*) and 2(*c*), the colour coding being the same. We note that the phase $\sin\Phi$ and drop radius R_D vary slightly between the traverses A–C but are assumed to be fixed in the orbital stability diagram.

wobbling orbits have been observed inside the green regions (Harris & Bush 2014). Moreover, there is experimental and numerical evidence of more complex periodic and quasiperiodic orbits within the green regions as the memory is further increased (Harris & Bush 2014; Oza *et al.* 2014*b*). The lateral extent of the unstable regions increases with increasing memory; consequently, virtually all of the orbital solutions become unstable in the high-memory limit $\gamma \to \gamma_F$. It is in this limit that a wave-like statistical behaviour emerges from a chaotic pilot-wave dynamics (Harris & Bush 2014; Oza *et al.* 2014*b*).

6. Discussion

We have developed and analysed an integro-differential trajectory equation that describes the pilot-wave dynamics of a walker in a rotating frame. The theoretical predictions for the walker's orbital radius r_0 and frequency ω agree well with the experimental results of Harris & Bush (2014). Specifically, our model allows us to rationalize the emergence of quantized orbits and wobbling states as the memory is increased progressively, as well as the relative absence of stable orbits in the high-memory limit. The theory also predicts the existence of trapped states, which are orbital solutions of small radius $r_0 \sim |\Omega_0 - \Omega|^{1/2}$ that arise for $\Omega \lesssim \Omega_0$.

In the low-orbital-memory regime, the walker is found to execute circular orbits of radius $r_0 = au_0/2\Omega$, where a is defined in terms of experimental parameters in (4.7). The factor a originates from the small radial component of the wave force, and can be interpreted in terms of an added mass associated with the walker's pilot-wave field. In the mid-memory regime, the orbital radii are found to be quantized. The orbital

quantization has been rationalized by analysing the stability of the orbital solutions. Orbits on the portions of the solution curves in figure 2(*a*,*c*) with positive slope are found to be unstable.

As the memory is increased further, the theory predicts the existence of self-orbiting solutions, even at $\Omega = 0$, wherein the wave force balances the centripetal force. Such self-orbiting states might represent a hydrodynamic analogue of a quantum spin state. Indeed, the self-orbiting solution is reminiscent of the Kerr–Newman model of the electron, in which the electron is modelled as a charged particle orbiting in its own wave field (Burinskii 2008). These hydrodynamic 'spin states' have not yet been observed in experiments, and are unstable according to linear stability theory; nevertheless, it is conceivable that they could be stabilized by nonlinear effects, a possibility to be explored elsewhere. When subjected to rotation, the solutions that co-rotate with the bath would have slightly larger orbital radii than their counter-rotating counterparts, an effect reminiscent of Zeeman splitting in quantum mechanics.

In the future, we will analyse the transition from simple orbital to chaotic dynamics in greater detail. There is evidence that Hopf-like bifurcations of the orbital solutions lead to wobbling orbits, as reported in § 5, which will be examined in Oza *et al.* (2014*b*). Higher-order instabilities may give rise to precessing orbits, intermittent wobbling, and complex quasiperiodic orbits, all of which have been observed either in our experiments (Harris & Bush 2014) or numerical simulations (Oza *et al.* 2014*b*). We will also analyse the statistical behaviour of the walker's motion, characterizing the emergence of wave-like statistics in the high-memory limit (Harris & Bush 2014; Oza *et al.* 2014*b*).

A similar approach will be applied to analysing walkers moving in a central force field, a configuration currently being examined experimentally by Couder and coworkers (Perrard *et al.* 2014). The integro-differential equation of motion has adequately captured the observed behaviour of a walker in a rotating frame; moreover, it has allowed us to make predictions that have been confirmed experimentally. Having benchmarked our pilot-wave model against experimental data in this configuration, our hope is that we may now apply it to systems that are not necessarily accessible in the laboratory.

Acknowledgements

The authors gratefully acknowledge the generous financial support of the NSF through Grant CBET-0966452, and RR partial support through grants DMS-1007967 and DMS-1115278. AO and DH also acknowledge support through the NSF Graduate Research Fellowship Program, and AO that of the Hertz Foundation. The authors also thank Jan Moláček, Yves Couder and Emmanuel Fort for valuable discussions.

Appendix A. Asymptotic expansion of (4.1) in the low-orbital-memory regime $|\hat{\omega}| \ll 1$

In § 4.1, we analysed the properties of orbital solutions in the low-orbital-memory regime $|\hat{\omega}| \ll 1$, approximating (4.1) by (4.2). This can be justified as follows. Due to the exponential terms in the integrands, the dominant contribution to the integrals in (4.1) comes from the region $z \sim O(1)$. We thus make the approximations $\sin(\hat{\omega}z/2) \approx \hat{\omega}z/2$, $\cos(\hat{\omega}z/2) \approx 1$ and $J_1\left(2\hat{r}_0 \sin(\hat{\omega}z/2)\right) \approx J_1\left(\hat{r}_0\hat{\omega}z\right)$, which are valid provided $|\hat{\omega}| \ll 1$ and $\hat{r}_0|\hat{\omega}|^3 \ll 1$. Nevertheless, we claimed that this approximation may be applied even for arbitrarily large values of $\hat{r}_0$. We here use a simplified set of equations to illustrate why this is the case.

For the remainder of this section, we understand the variables to be non-dimensional and drop all carets. We consider the equations

$$\left.\begin{aligned} -\kappa r_0\omega^2 - \Omega r_0\omega &= \beta\int_0^\infty J_1\left(r_0\omega z - \frac{r_0\omega^3 z^3}{24}\right)\frac{\omega z}{2}\mathrm{e}^{-z}\,\mathrm{d}z,\\ r_0\omega &= \beta\int_0^\infty J_1\left(r_0\omega z - \frac{r_0\omega^3 z^3}{24}\right)\mathrm{e}^{-z}\,\mathrm{d}z. \end{aligned}\right\} \tag{A 1}$$

These equations are more tractable than (4.1) and have the same qualitative behaviour, so we use them to illustrate why the low-orbital-memory approximation (4.2) is valid for arbitrarily large values of r_0.

Assuming that $u = r_0\omega$ is bounded, we may Taylor expand the Bessel function, since $|\omega| \ll 1$ and $z \sim O(1)$. We thus obtain

$$\begin{aligned} J_1\left(r_0\omega z - \frac{r_0\omega^3 z^3}{24}\right) &= J_1(r_0\omega z) + \sum_{n=1}^{\infty}\frac{(-1)^n}{n!}J_1^{(n)}(r_0\omega z)\left(\frac{r_0\omega^3 z^3}{24}\right)^n\\ &= J_1(uz) + \sum_{n=1}^{\infty}\frac{(-1)^n\omega^{2n}u^n}{24^n n!}J_1^{(n)}(uz)z^{3n}, \end{aligned} \tag{A 2}$$

which yields the asymptotic expansion

$$\int_0^\infty J_1\left(r_0\omega z - \frac{r_0\omega^3 z^3}{24}\right)\frac{\omega z}{2}\mathrm{e}^{-z}\,\mathrm{d}z = \frac{u\omega}{2\left(1+u^2\right)^{3/2}} + \mathscr{R}_1, \tag{A 3a}$$

$$\int_0^\infty J_1\left(r_0\omega z - \frac{r_0\omega^3 z^3}{24}\right)\mathrm{e}^{-z}\,\mathrm{d}z = \frac{1}{u}\left(1 - \frac{1}{\sqrt{1+u^2}}\right) + \mathscr{R}_2, \tag{A 3b}$$

where

$$\mathscr{R}_1 \sim \frac{\omega}{2}\sum_{n=1}^{\infty}\frac{(-1)^n\omega^{2n}u^n}{24^n n!}\int_0^\infty J_1^{(n)}(uz)z^{3n+1}\mathrm{e}^{-z}\,\mathrm{d}z, \tag{A 4a}$$

$$\mathscr{R}_2 \sim \sum_{n=1}^{\infty}\frac{(-1)^n\omega^{2n}u^n}{24^n n!}\int_0^\infty J_1^{(n)}(uz)z^{3n}\mathrm{e}^{-z}\,\mathrm{d}z. \tag{A 4b}$$

As shown at the conclusion of this appendix, the integrals in $\mathscr{R}_1$ and $\mathscr{R}_2$ may be evaluated exactly, yielding

$$\begin{aligned} \mathscr{R}_1 &\sim \frac{\omega}{2u}\sum_{n=1}^{\infty}\frac{(-1)^{n+1}(3n+1)!\omega^{2n}}{24^n n!}\sum_{j=0}^{n+1}(-1)^j\binom{n+1}{j}\frac{P_{3n+1-j}\left(1/\sqrt{1+u^2}\right)}{(1+u^2)^{(3n+2-j)/2}}\\ &= \frac{\omega}{2u}\sum_{n=1}^{\infty}\omega^{2n}R_1^{(n)}, \end{aligned} \tag{A 5a}$$

$$\begin{aligned} \mathscr{R}_2 &\sim \frac{1}{u}\sum_{n=1}^{\infty}\frac{(-1)^{n+1}(3n)!\omega^{2n}}{24^n n!}\sum_{j=0}^{n+1}(-1)^j\binom{n+1}{j}\frac{P_{3n-j}\left(1/\sqrt{1+u^2}\right)}{(1+u^2)^{(3n+1-j)/2}}\\ &= \frac{1}{u}\sum_{n=1}^{\infty}\omega^{2n}R_2^{(n)}, \end{aligned} \tag{A 5b}$$

where P_k is the Legendre polynomial of order k. Note that $1/\sqrt{1+u^2} \leqslant 1$ for all u, so $|P_k| \leqslant c_k$ for some constants c_k. Using the triangle inequality and the formula $\sum_{j=0}^{n+1} \binom{n+1}{j} x^{j/2} = \left(1+\sqrt{x}\right)^{n+1}$, we obtain the upper bound

$$\left|R_1^{(n)}\right| \leqslant \frac{f_n(1+\sqrt{1+u^2})^{n+1}}{(1+u^2)^{(3n+2)/2}}, \quad \left|R_2^{(n)}\right| \leqslant \frac{g_n(1+\sqrt{1+u^2})^{n+1}}{(1+u^2)^{(3n+1)/2}} \tag{A 6}$$

for some constants f_n, g_n. This shows that (A5) is well ordered even for large u, which suggests that the asymptotic expansion is valid for all u.

We now justify (A5). Using the fact that $J_1(x) = -J_0'(x)$, we integrate (A4) by parts $n+1$ times to obtain

$$\mathscr{R}_1 \sim \frac{\omega}{2u} \sum_{n=1}^{\infty} \frac{\omega^{2n}}{24^n n!} \int_0^{\infty} J_0(uz) \frac{\mathrm{d}^{n+1}}{\mathrm{d}z^{n+1}} \left(z^{3n+1} \mathrm{e}^{-z}\right) \mathrm{d}z, \tag{A 7a}$$

$$\mathscr{R}_2 \sim \frac{1}{u} \sum_{n=1}^{\infty} \frac{\omega^{2n}}{24^n n!} \int_0^{\infty} J_0(uz) \frac{\mathrm{d}^{n+1}}{\mathrm{d}z^{n+1}} \left(z^{3n} \mathrm{e}^{-z}\right) \mathrm{d}z. \tag{A 7b}$$

For integers $k < m$, we have the formula

$$\frac{\mathrm{d}^k}{\mathrm{d}z^k}\left(z^m \mathrm{e}^{-z}\right) = (-1)^k \mathrm{e}^{-z} \sum_{j=0}^{k} (-1)^j \binom{k}{j} \frac{m!}{(m-j)!} z^{m-j}, \tag{A 8}$$

and so obtain

$$\begin{aligned} \mathscr{R}_1 \sim{}& \frac{\omega}{2u} \sum_{n=1}^{\infty} \frac{(-1)^{n+1}\omega^{2n}}{24^n n!} \sum_{j=0}^{n+1} (-1)^j \binom{n+1}{j} \frac{(3n+1)!}{(3n+1-j)!} \\ &\times \int_0^{\infty} J_0(uz) z^{3n+1-j} \mathrm{e}^{-z} \mathrm{d}z, \end{aligned} \tag{A 9a}$$

$$\begin{aligned} \mathscr{R}_2 \sim{}& \frac{1}{u} \sum_{n=1}^{\infty} \frac{(-1)^{n+1}\omega^{2n}}{24^n n!} \sum_{j=0}^{n+1} (-1)^j \binom{n+1}{j} \frac{(3n)!}{(3n-j)!} \\ &\times \int_0^{\infty} J_0(uz) z^{3n-j} \mathrm{e}^{-z} \mathrm{d}z. \end{aligned} \tag{A 9b}$$

The integrals above can be evaluated in closed form using the formula (Bateman 1944)

$$\int_0^{\infty} J_0(uz) z^k \mathrm{e}^{-z} \mathrm{d}z = k! \frac{P_k\left(1/\sqrt{1+u^2}\right)}{\left(1+u^2\right)^{(k+1)/2}}, \tag{A 10}$$

from which we obtain (A5).

Appendix B. Evaluation of integral terms in $F_1(s), F_2(s), G_1(s), G_2(s)$

We evaluate some of the integrals appearing in the definition (5.6) of the functions $F_1(s)$, $F_2(s)$, $G_1(s)$ and $G_2(s)$, by repeatedly employing the fact that r_0 and ω are defined as the solution to (4.1):

$$\begin{aligned}\mathscr{I}[f(t)\sin\omega t] &= \int_0^\infty \frac{J_1(2r_0\sin(\omega z/2))}{2r_0\sin(\omega z/2)}\sin\omega z\mathrm{e}^{-z}\,\mathrm{d}z\\ &= \int_0^\infty \frac{J_1(2r_0\sin(\omega z/2))}{r_0}\cos\frac{\omega z}{2}\mathrm{e}^{-z}\,\mathrm{d}z = \frac{\omega}{\beta}. \qquad \text{(B 1)}\\ \mathscr{I}[g(t)\sin\omega t] &= \int_0^\infty J_1'\left(2r_0\sin\frac{\omega z}{2}\right)\sin\omega z\mathrm{e}^{-z}\,\mathrm{d}z\\ &= 2\int_0^\infty J_1'\left(2r_0\sin\frac{\omega z}{2}\right)\cos\frac{\omega z}{2}\sin\frac{\omega z}{2}\mathrm{e}^{-z}\,\mathrm{d}z\\ &= \frac{2}{r_0\omega}\int_0^\infty\left[J_1\left(2r_0\sin\frac{\omega z}{2}\right)\sin\frac{\omega z}{2}-\frac{\omega}{2}J_1\left(2r_0\sin\frac{\omega z}{2}\right)\cos\frac{\omega z}{2}\right]\mathrm{e}^{-z}\,\mathrm{d}z\\ &= -\frac{2}{\beta}\left[\kappa\omega+\Omega+\frac{\omega}{2}\right], \qquad \text{(B 2)}\end{aligned}$$

where we integrate by parts in the third line. Combining (B 1) and (B 2), we obtain

$$\frac{1}{2}\left(\mathscr{I}[f(t)\sin\omega t]+\mathscr{I}[g(t)\sin\omega t]\right) = -\frac{\kappa\omega+\Omega}{\beta}, \qquad \text{(B 3}a\text{)}$$

$$\frac{1}{2}\left(\mathscr{I}[g(t)\sin\omega t]-\mathscr{I}[f(t)\sin\omega t]\right) = -\frac{\kappa\omega+\omega+\Omega}{\beta}, \qquad \text{(B 3}b\text{)}$$

which appear in $F_2(s)$ and $G_1(s)$, respectively. Similarly,

$$\mathscr{I}\left[f(t)\sin^2\frac{\omega t}{2}\right] = \int_0^\infty \frac{J_1(2r_0\sin(\omega z/2))}{2r_0}\sin\frac{\omega z}{2}\mathrm{e}^{-z}\,\mathrm{d}z = -\frac{\kappa\omega^2+\Omega\omega}{2\beta} \qquad \text{(B 4)}$$

$$\begin{aligned}\mathscr{I}\left[g(t)\cos^2\frac{\omega t}{2}\right] &= \int_0^\infty J_1'\left(2r_0\sin\frac{\omega z}{2}\right)\cos\frac{\omega z}{2}\cos\frac{\omega z}{2}\mathrm{e}^{-z}\,\mathrm{d}z\\ &= \frac{1}{r_0\omega}\int_0^\infty\left[\frac{\omega}{2}J_1\left(2r_0\sin\frac{\omega z}{2}\right)\sin\frac{\omega z}{2}\mathrm{e}^{-z}\right.\\ &\quad\left.+\,J_1\left(2r_0\sin\frac{\omega z}{2}\right)\cos\frac{\omega z}{2}\mathrm{e}^{-z}\right]\mathrm{d}z\\ &= \frac{1}{\beta}\left[-\frac{1}{2}(\kappa\omega^2+\Omega\omega)+1\right], \qquad \text{(B 5)}\end{aligned}$$

where we integrate by parts in the second line. Combining (B 4) and (B 5), we obtain

$$\mathscr{I}\left[g(t)\cos^2\frac{\omega t}{2}\right]-\mathscr{I}\left[f(t)\sin^2\frac{\omega t}{2}\right] = \frac{1}{\beta}, \qquad \text{(B 6)}$$

which appears in $G_2(s)$.

There do not appear to be simple expressions for the terms $\mathscr{I}\left[f(t)\cos^2(\omega t/2)\right]$ and $\mathscr{I}\left[g(t)\sin^2(\omega t/2)\right]$ that appear in $F_1(s)$.

Appendix C. Proof that $F_0(r_0) = r_0\omega d_1(\mathrm{d}\Omega/\mathrm{d}r_0)$

We first expand the functions (5.8) around $s=0$ and obtain $A(s)=a_0+O(s)$, $B(s)=b_1s+O(s^2)$, $C(s)=c_0+O(s)$ and $D(s)=d_1s+O(s^2)$, where

$$\left.\begin{aligned} a_0 &= -\left(\kappa\omega^2 + \Omega\omega + 2\beta\mathscr{I}\left[g(t)\sin^2\frac{\omega t}{2}\right]\right), \quad b_1 = 2\omega\kappa + \Omega + \frac{\beta}{2}\mathscr{I}\left[(f(t)+g(t))\,t\sin\omega t\right] \\ c_0 &= 2\left[\omega\left(1+\kappa\right)+\Omega\right], \quad d_1 = 1+\beta\mathscr{I}\left[\left(f(t)\sin^2\frac{\omega t}{2} - g(t)\cos^2\frac{\omega t}{2}\right)t\right]. \end{aligned}\right\} \tag{C 1}$$

Thus, $F_0(r_0) = a_0 d_1 + b_1 c_0$.

We now deduce an equation for $\mathrm{d}\Omega/\mathrm{d}r_0$ by first differentiating the governing equations (4.1) with respect to r_0:

$$\begin{aligned} 2\omega\kappa\frac{\mathrm{d}\omega}{\mathrm{d}r_0} + \omega\frac{\mathrm{d}\Omega}{\mathrm{d}r_0} + \Omega\frac{\mathrm{d}\omega}{\mathrm{d}r_0} &= -2\beta\mathscr{I}\left[\left(\frac{\partial f}{\partial r_0} + \frac{\partial f}{\partial\omega}\frac{\mathrm{d}\omega}{\mathrm{d}r_0}\right)\sin^2\frac{\omega t}{2}\right. \\ &\quad \left. + \frac{\mathrm{d}\omega}{\mathrm{d}r_0}\frac{t}{2}f(t)\sin\omega t\right] \qquad (\mathrm{C}\,2a) \\ \frac{\mathrm{d}\omega}{\mathrm{d}r_0} &= \beta\mathscr{I}\left[\frac{\mathrm{d}\omega}{\mathrm{d}r_0}tf(t)\cos\omega t + \left(\frac{\partial f}{\partial r_0} + \frac{\partial f}{\partial\omega}\frac{\mathrm{d}\omega}{\mathrm{d}r_0}\right)\sin\omega t\right]. \qquad (\mathrm{C}\,2b) \end{aligned}$$

Since

$$\frac{\partial f}{\partial r_0} = \frac{1}{r_0}\left(g(t) - f(t)\right), \quad \frac{\partial f}{\partial\omega} = \frac{t}{2}\cot\frac{\omega t}{2}\left(g(t) - f(t)\right), \tag{C 3}$$

we deduce that

$$\begin{aligned} \frac{\mathrm{d}\omega}{\mathrm{d}r_0}\left(2\omega\kappa + \Omega\right) + \omega\frac{\mathrm{d}\Omega}{\mathrm{d}r_0} &= \frac{2\beta}{r_0}\mathscr{I}\left[\left(f(t) - g(t)\right)\sin^2\frac{\omega t}{2}\right] \\ &\quad - \frac{\beta}{2}\mathscr{I}\left[\left(f(t)+g(t)\right)t\sin\omega t\right]\frac{\mathrm{d}\omega}{\mathrm{d}r_0} \qquad (\mathrm{C}\,4a) \\ \frac{\beta}{r_0}\mathscr{I}\left[\left(g(t) - f(t)\right)\sin\omega t\right] &= \frac{\mathrm{d}\omega}{\mathrm{d}r_0}\left(1 - \beta\mathscr{I}\left[\left(g(t)\cos^2\frac{\omega t}{2} - f(t)\sin^2\frac{\omega t}{2}\right)t\right]\right). \qquad (\mathrm{C}\,4b) \end{aligned}$$

Some of the integrals can be simplified using the results in appendix B, yielding

$$\begin{aligned} -\omega\frac{\mathrm{d}\Omega}{\mathrm{d}r_0} &= \frac{\mathrm{d}\omega}{\mathrm{d}r_0}\left(2\omega\kappa + \Omega + \frac{\beta}{2}\mathscr{I}\left[\left(f(t)+g(t)\right)t\sin\omega t\right]\right) \\ &\quad + \frac{2\beta}{r_0}\mathscr{I}\left[g(t)\sin^2\frac{\omega t}{2}\right] + \frac{1}{r_0}\left(\kappa\omega^2 + \Omega\omega\right) \qquad (\mathrm{C}\,5a) \\ -\frac{2}{r_0}\left(\omega\left(1+\kappa\right)+\Omega\right) &= \frac{\mathrm{d}\omega}{\mathrm{d}r_0}\left(1 - \beta\mathscr{I}\left[\left(g(t)\cos^2\frac{\omega t}{2} - f(t)\sin^2\frac{\omega t}{2}\right)t\right]\right). \\ &\qquad (\mathrm{C}\,5b) \end{aligned}$$

Using (C 1), these equations can be written as

$$a_0 - r_0 b_1\frac{\mathrm{d}\omega}{\mathrm{d}r_0} = r_0\omega\frac{\mathrm{d}\Omega}{\mathrm{d}r_0}, \quad c_0 + r_0 d_1\frac{\mathrm{d}\omega}{\mathrm{d}r_0} = 0. \tag{C 6}$$

We eliminate $\mathrm{d}\omega/\mathrm{d}r_0$, yielding an equation for $\mathrm{d}\Omega/\mathrm{d}r_0$:

$$a_0 + \frac{b_1 c_0}{d_1} = r_0\omega\frac{\mathrm{d}\Omega}{\mathrm{d}r_0}, \tag{C 7}$$

which is valid since $d_1 > 0$ (Oza *et al.* 2014*a*). We thus obtain the desired result

$$F_0(r_0) = r_0\omega d_1\frac{\mathrm{d}\Omega}{\mathrm{d}r_0}. \tag{C 8}$$

REFERENCES

BACCIAGALUPPI, G. & VALENTINI, A. 2009 *Quantum Theory at the Crossroads: Reconsidering the 1927 Solvay Conference*. Cambridge University Press.

BATEMAN, H. 1944 *Partial Differential Equations of Mathematical Physics*. Dover.

BELL, J. S. 1988 *Speakable and Unspeakable in Quantum Mechanics*. Cambridge University Press.

DE BROGLIE, L. 1926 *Ondes et Mouvements*. Gauthier-Villars.

DE BROGLIE, L. 1987 Interpretation of quantum mechanics by the double solution theory. *Ann. Fond. Louis de Broglie* **12** (4), 1–23.

BURINSKII, A. 2008 The Dirac–Kerr–Newman electron. *Grav. Cosmol.* **40** (2), 109–122.

BUSH, J. W. M. 2010 Quantum mechanics writ large. *Proc. Natl Acad. Sci. USA* **107** (41), 17455–17456.

COHEN-TANNOUDJI, C., DIU, B. & LALOË, F. 1977 *Quantum Mechanics*. John Wiley & Sons.

COUDER, Y. & FORT, E. 2006 Single-particle diffraction and interference at a macroscopic scale. *Phys. Rev. Lett.* **97**, 154101.

COUDER, Y., PROTIÈRE, S., FORT, E. & BOUDAOUD, A. 2005 Walking and orbiting droplets. *Nature* **437**, 208.

CROMMIE, M., LUTZ, C. & EIGLER, D. 1993 Confinement of electrons to quantum corrals on a metal surface. *Science* **262**, 5131.

EDDI, A., FORT, E., MOISY, F. & COUDER, Y. 2009 Unpredictable tunnelling of a classical wave-particle association. *Phys. Rev. Lett.* **102**, 240401.

EDDI, A., MOUKHTAR, J., PERRARD, S., FORT, E. & COUDER, Y. 2012 Level splitting at macroscopic scale. *Phys. Rev. Lett.* **108**, 264503.

EDDI, A., SULTAN, E., MOUKHTAR, J., FORT, E., ROSSI, M. & COUDER, Y. 2011 Information stored in Faraday waves: the origin of path memory. *J. Fluid Mech.* **675**, 433–463.

FORT, E., EDDI, A., BOUDAOUD, A., MOUKHTAR, J. & COUDER, Y. 2010 Path-memory induced quantization of classical orbits. *Proc. Natl Acad. Sci. USA* **107** (41), 17515–17520.

HARRIS, D. M. & BUSH, J. W. M. 2014 Droplets walking in a rotating frame: from quantized orbits to multimodal statistics. *J. Fluid Mech.* **739**, 444–464.

HARRIS, D. M., MOUKHTAR, J., FORT, E., COUDER, Y. & BUSH, J. W. M. 2013 Wavelike statistics from pilot-wave dynamics in a circular corral. *Phys. Rev.* E **88**, 011001.

KUMAR, K. 1996 Linear theory of Faraday instability in viscous fluids. *Proc. R. Soc. Lond.* A **452**, 1113–1126.

MOLÁČEK, J. & BUSH, J. W. M. 2013*a* Drops bouncing on a vibrating bath. *J. Fluid Mech.* **727**, 582–611.

MOLÁČEK, J. & BUSH, J. W. M. 2013*b* Drops walking on a vibrating bath: towards a hydrodynamic pilot-wave theory. *J. Fluid Mech.* **727**, 612–647.

OZA, A. U., BUSH, J. W. M. & ROSALES, R. R. 2014*a* Orbital stability in hydrodynamic pilot-wave theory (in preparation).

OZA, A. U., ROSALES, R. R. & BUSH, J. W. M. 2013 A trajectory equation for walking droplets: hydrodynamic pilot-wave theory. *J. Fluid Mech.* **737**, 552–570.

OZA, A. U., WIND-WILLASSEN, Ø., HARRIS, D. M., ROSALES, R. R. & BUSH, J. W. M. 2014*b* Pilot-wave hydrodynamics in a rotating frame: exotic orbits. *Physics of Fluids* (submitted).

PERRARD, S., LABOUSSE, M., MISKIN, M., FORT, E. & COUDER, Y. 2014 Self-organization into quantized eigenstates of a classical wave-driven particle. *Nature Commun.* **5**, 3219.

PROTIÈRE, S., BOUDAOUD, A. & COUDER, Y. 2006 Particle-wave association on a fluid interface. *J. Fluid Mech.* **554**, 85–108.

WALKER, J. 1978 Drops of liquid can be made to float on the liquid. What enables them to do so? *Sci. Am.* **238** (6), 151–158.

WATSON, G. N. 1966 *A Treatise on the Theory of Bessel Functions*. 2nd edn. Cambridge University Press.

WEINSTEIN, A. & POUNDER, J. R. 1945 An electromagnetic analogy in mechanics. *Am. Math. Mont.* **52** (8), 432–438.

WIND-WILLASSEN, Ø., MOLÁČEK, J., HARRIS, D. M. & BUSH, J. W. M. 2013 Exotic states of bouncing and walking droplets. *Phys. Fluids* **25**, 082002.